Key Points:

- Best fit model produces satisfactory fits to all three data sets
- Elongate chambers of volume 64–256 km^3 with centroid at 9–17 km depth are preferred
- Magma permeability, radius, and friction are lower than estimates from inversions with the steady-state model

Correspondence to:
Y.-Q. Wong,
Ying-Qi.Wong@glasgow.ac.uk

Joint Inversions of Ground Deformation, Extrusion Flux, and Gas Emissions Using Physics-Based Models for the Mount St. Helens 2004–2008 Eruption

Ying-Qi Wong[1] (ID) **and Paul Segall[2]** (ID)

[1]School of Geographical and Earth Sciences, University of Glasgow, Glasgow, UK, [2]Department of Geophysics, Stanford University, Stanford, CA, USA

Abstract With the increasing quantity and quality of data collected at volcanoes, there is growing potential to incorporate all the data into analyses of magmatic systems. Physics-based models provide a natural and meaningful way to bring together real-time monitoring data and laboratory analyses of eruption products, with the goal of better understanding volcanic processes. We develop a framework for joint inversions of diverse time series data using the physics-based model for dome-forming eruptions from Wong and Segall (2019, https://doi.org/10.1029/2019JB017585). Applying this method to the 2004–2008 eruption at Mount St. Helens, we estimate essential system parameters, including chamber geometry, pressure, volatile content, and material properties, from extruded volume, ground deformation, and carbon dioxide emissions time series. The model parameter space is first sampled using the neighborhood search algorithm (Sambridge, 1999b, https://doi.org/10.1046/j.1365-246X.1999.00876.x). The resulting ensemble of models is resampled to generate posterior probability density functions on the parameters (Sambridge, 1999a, https://doi.org/10.1046/j.1365-246x.1999.00900.x). We find models that fit all three data sets well. Posterior probability density functions suggest an elongate chamber with aspect ratio less than 0.55, located at 9–17 km depth. Since the model calculates pressure change during the eruption, we can constrain chamber volume to 64–256 km^3. Volume loss in the chamber during the eruption is 20–66 million m^3. At the top of the chamber, total (dissolved and exsolved) water contents are 5.0–6.4 wt% and total carbon dioxide contents are 1,600–3,900 ppm, giving a porosity of 5%–16% depending on the conduit length. Compared to previous inversions using a steady-state conduit model, we obtain a lower magma permeability scale, radius, and friction coefficient.

Plain Language Summary Data collected from volcanoes shed light on the structure of the subsurface storage chamber and the migration of magma, thereby enhancing our understanding of volcanic hazards. Integrating multiple data sets into analyses of a single eruption can resolve more details of the volcanic system. A theoretical model that predicts these data given some input parameters is needed to connect diverse volcanological data sets. We have previously constructed a physics-based model that simulates the ascent of magma from a storage chamber to the surface through a pipe. The model is specialized for lava dome eruptions, such as the 2004–2008 Mount St. Helens eruption, by taking into account magma solidification, gases coming out of solution and gases escaping from the system. The model is used to calculate the lava dome volume, deformation of the land surface (detected by Global Positioning System) and rate of gas emissions. The model has several unknown parameters. We run 120,000 iterations of the model with different combinations of input parameters to look for combinations that fit all three data sets. This approach can constrain chamber geometry, pressure, gas content, and material properties. Insights into this variety of system parameters would not have been possible with standard discipline-specific modeling.

1. Introduction

In the past few decades, the expansion of both ground and satellite-based monitoring systems, as well as advances in laboratory techniques to study volcanic products, have increased the quantity and quality of volcanological data. Since these observations are produced by common physical processes, physics-based models can provide a natural and meaningful way to bring together these diverse data, at the same time improving our understanding of volcanic processes.

A subset of models examines the last stages of magma's ascent through a volcanic conduit to the surface. These conduit flow models apply magma rheologic models to fundamental conservation laws to simulate magma flow from chamber to surface. Phase changes affect magma properties such as density and viscosity which in turn regulate magma flux (e.g., Gonnermann & Manga, 2007). Models with varying levels of complexity have been developed to investigate the processes controlling effusive and explosive behavior, as well as to study both steady-state and time-varying conduit flow (e.g., De' Michieli Vitturi et al., 2013; Denlinger & Hoblitt, 1999; Jaupart & Allègre, 1991; Mastin, 2002; Papale, 2001). These studies have elucidated critical processes that determine eruption style and duration, such as the complex feedbacks between magma velocity and crystallization kinetics or gas escape that may produce cyclic lava discharge (Kozono & Koyaguchi, 2012; Melnik & Sparks, 2005). Connections to observations mainly involve qualitative comparisons between observed and predicted magma flux, which is a direct model output. A few studies have gone further to couple conduit models to the surrounding crust to compare with observed ground deformation (e.g., Albino et al., 2011; Anderson & Segall, 2011; Kawaguchi & Nishimura, 2015; Neuberg et al., 2018).

Prior work by Anderson and Segall (2013) demonstrated the utility of physics-based volcanic models in joint inversions of geophysical data sets. Their study focused on eruptions that produce a lava dome at the surface. The 1D model simulates ascent of a three-phase magma, taking into account gas solubility and its effect on viscosity. Ascending magma causes the pressure in the chamber to drop, decreasing flow velocity exponentially in time. Model outputs were compared with extruded volume and geodetic data from the 2004–2008 eruption at Mount St. Helens using the Markov Chain Monte Carlo (MCMC) algorithm. Since conduit models can be highly nonlinear, this probabilistic approach captures the range of model parameters consistent with the observations. Compared with traditional geodetic inversions, incorporating the physics-based model with extruded volume data allowed more parameters to be constrained, including initial chamber pressure, dissolved volatile content, and magma and chamber compressibility. The physics-based model is the crucial link that ties these data sets together.

In order to harness the full power of joint inversions using physics-based models, we need to capture the essential physical processes in the magmatic system. For dome-forming eruptions, slow ascent allows magma to crystallize gradually, an effect greatly simplified in the model of Anderson and Segall (2013). Gases exsolving during ascent may escape from the magma, which, together with crystallization, is critical to forming dense, degassed plugs in the shallow reaches of conduits (e.g., Clarke et al., 2007; Diller et al., 2006; Kozono & Koyaguchi, 2012; Schneider et al., 2012). Wong et al. (2017) developed a steady-state physics-based model which incorporated crystallization and gas escape to study the quasisteady phase of the 2004–2008 Mount St. Helens eruption, when magma flux was approximately constant. Diverse data, including magma flux, dome rock porosity, solidus depth, and plug depth, were used to derive distributions of critical system parameters. Wong and Segall (2019) extended this conduit model to study the temporal evolution of conduit flow. Scaling analysis showed that when chamber pressure declines at a rate comparable to magma ascent, such as in dome-forming eruptions, transient effects can become important. Steady-state solutions would be inadequate in modeling the initial decline in magma flux; instead time-dependent solutions are needed. In addition, transient effects do not have simple relationships with their corresponding steady-state solutions. For example, depending on the magma permeability model, transient effects may increase or decrease the magma flux relative to steady-state solutions. Qualitative comparisons of time-dependent model predictions with extruded volume, ground deformation, and gas emissions time series from Mount St. Helens elucidated the parameters that influence the temporal evolution of dome-forming eruptions.

In this study, we develop a framework for quantitative joint inversions of diverse time series data sets using the time-dependent conduit flow model from Wong and Segall (2019). Given extruded volume, ground deformation, and carbon dioxide emissions time series from the 2004–2008 Mount St. Helens eruption, we estimate essential system properties including chamber geometry, initial pressure, volatile content, and material properties. A suitable inversion technique for physics-based models should account for the nonlinearity of volcanic systems, therefore we prefer probabilistic methods that estimate not only an optimal solution but also the range of admissible solutions (Sparks, 2003). At the same time, since the model is computationally expensive, we are unable to use simple stochastic methods such as MCMC that require
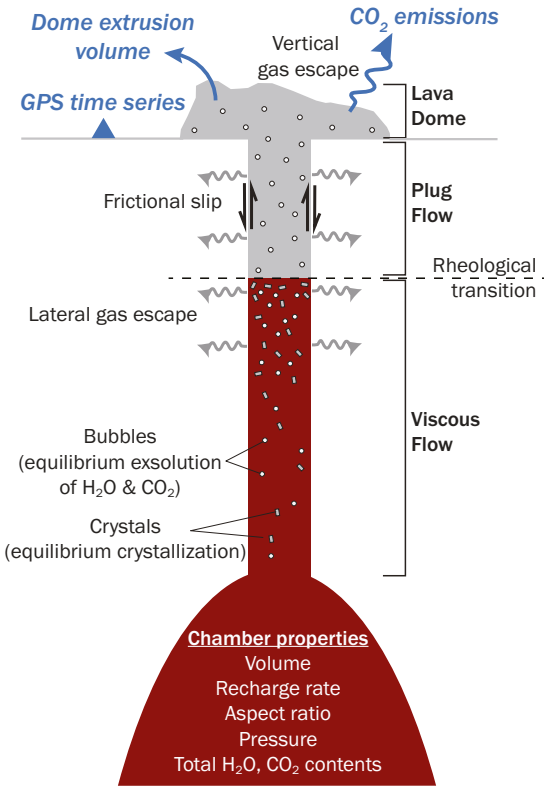
Figure 1. Model setup adapted from Wong and Segall (2019). Magma ascends viscously from a chamber through a cylindrical conduit, where it undergoes crystallization, gas exsolution, and gas escape, eventually transitioning to a solid plug that slides along the conduit walls. The three data sets used to constrain model parameters are shown in blue.

millions of forward model evaluations. Based on these considerations, we apply the Neighborhood Algorithm which is trivially parallelizable and can build probability density functions (PDFs) of the relevant system parameters (Sambridge, 1999b, 1999a).

2. Methods

2.1. Physics-Based Model for Mount St. Helens Plumbing System

We have developed a physics-based model of the plumbing system at Mount St. Helens to simulate magma ascent from an ellipsoidal magma chamber through a conduit to the surface (Figure 1). The model is one-dimensional (radially averaged) and isothermal. Properties in the chamber are taken as lumped parameters evolving with time, while properties in the conduit are modeled in both time and depth. In this section, we present a brief overview of the chamber-conduit model; details can be found in Wong and Segall (2019).

At the beginning of the eruption, pressure in the chamber exceeds the magma column weight and drives flow out of the chamber toward the surface. The ascending magma exsolves volatiles and crystallizes. Once enough volatiles exsolve, the gas volume fraction exceeds the percolation threshold and permits gases to escape from the system both vertically through the conduit and laterally through the conduit walls. The combined effects of gas exsolution, gas escape, and crystallization strongly influence viscosity and cause the magma flow regime to evolve naturally from viscous flow at depth to solid plug sliding in the shallow part of the conduit. Removal of magma from the chamber decreases the chamber volume and pressure over time, which decreases the magma ascent velocity asymptotically toward zero.

2.1.1. Conduit Flow Model

Magma consists of solids, liquid melt which contains dissolved water (H_2O) and carbon dioxide (CO_2), and exsolved volatiles, giving its density ρ (symbols given in Table 1),

$$\rho = \rho_s \phi_s + \rho_l \phi_l c_1 + \rho_g \phi_g. \tag{1}$$

For each phase, the density and volume fraction are ρ and ϕ respectively. Subscripts indicate the phase: s for solids, l for liquid melt, and g for gases. The term c_1 accounts for dissolved volatiles and depends on the dissolved mass concentrations of H_2O and CO_2 $\left(\chi_h^d, \chi_c^d\right)$, which are modeled at equilibrium as functions of pressure and temperature using the solubility relations from Liu et al. (2005).

The solid fraction is assumed to be at equilibrium: it depends only on pressure and temperature. Crystallization kinetics are neglected due to the low ascent rate. We employ the isothermal equilibrium crystallization model from Schneider et al. (2012), which is calculated from the MELTS thermodynamic model (Ghiorso & Sack, 1995) for the water-saturated Mount St. Helens dacite chemical composition (Pallister et al., 2008). The crystallization model is converted to a piecewise polynomial to estimate the mass and volume fraction of the solid at a given pressure and temperature, here assumed constant at 850°C.

These component phases affect magma viscosity η, which is a combination of the melt viscosity η_m and the relative viscosity increase due to solids η_s,

$$\eta = \eta_m \left(\chi_h^d, \chi_c^d, T\right) \eta_s \left(\phi_s, \dot{\gamma}\right). \tag{2}$$

Table 1
Symbols Describing Components of the Physics-Based Model

	Symbol description
Model parameters	
α	Magma chamber aspect ratio (width/height)
V_0	Magma chamber volume
Ω	Magma chamber recharge rate
L	Conduit length
R	Conduit radius
k_c	Scaling factor for magma permeability
ϕ_{gc}	Percolation threshold
f_0	Nominal coefficient of friction
a	Rate-dependence of friction
Δp_0	Excess pressure at conduit base at $t = 0$
χ_h^{ch}	Total H_2O content at conduit base
χ_c^{ch}	Total CO_2 content at conduit base
Prescribed parameters	
g	Gravitational acceleration (9.81 m/s²)
k_{wall}^{top}	Wall-rock permeability at surface (10^{-14} m²)
$\mathcal{M}_c$	Molar mass of CO_2 (44.01 g/mol)
$\mathcal{M}_h$	Molar mass of H_2O (18.02 g/mol)
p_{atm}	Atmospheric pressure (0.1 MPa)
R_c	Gas constant of CO_2 (188.9 J/kg K)
R_w	Gas constant of H_2O (461.5 J/kg K)
T	Temperature of magma (850°C)
v_r	Reference velocity for friction (10^{-5} m/s)
η_g	Gas viscosity (10^{-4} Pa s)
μ	Shear modulus of crust (20 GPa)
ρ_l	Density of melt (2,200 kg/m³)
ρ_s	Density of solids (2,600 kg/m³)
ρ_c^d	Density of dissolved CO_2 (2,200 kg/m³)
ρ_h^d	Density of dissolved H_2O (2,200 kg/m³)
ρ_{hyd}	Density of water (1,000 kg/m³)
ρ_{lith}	Density of host rock (2,700 kg/m³)
Field variables in numerical solution	
p	Pressure
v	Velocity
ϕ_g	Gas volume fraction
m_h	Mole fraction of exsolved H_2O
Other dependent variables	
c_1	Relationship between χ_c^d, χ_h^d and ϕ_l
k_{mag}	Magma permeability

We apply the dacite melt viscosity model of Whittington et al. (2009), which depends on dissolved volatile content and temperature T. For the relative viscosity increase due to solids, we apply the model of Costa (2005) and Caricchi et al. (2007) which incorporates a dependence on strain rate $\dot{\gamma}$. The effect of bubbles on viscosity is neglected since porosity of the 2004–2008 Mount St. Helens dome lavas is relatively low, thus the effect of crystals predominates (Llewellin & Manga, 2005).

Applying these magma properties, the governing equations for 1D conduit flow are

$$v = v_{visc} + v_{fric} = \frac{\tau_R R}{4\eta} + 2v_r \exp\left(-\frac{f_0}{a}\right)\sinh\left(\frac{\tau_R}{a\sigma_c}\right),$$
$$where\ \tau_R = -\frac{R}{2}\left(\frac{\partial p}{\partial z} + \rho g\right) \tag{3}$$

$$\frac{\partial}{\partial t}\left(\rho_s\phi_s + \rho_l\phi_l\right) = -\frac{\partial}{\partial z}\left[\left(\rho_s\phi_s + \rho_l\phi_l\right)v\right] \tag{4}$$

$$\frac{\partial}{\partial t}\left(\chi_h^d \rho_l\phi_l c_1 + \frac{1}{1+\Gamma}\rho_g\phi_g\right) = -\frac{\partial}{\partial z}\left[\left(\chi_h^d \rho_l\phi_l c_1 + \frac{1}{1+\Gamma}\rho_g\phi_g\right)v\right.$$
$$\left. + \frac{1}{1+\Gamma}\rho_g\phi_g\left(v_g - v\right)\right] - \frac{2\rho_g\phi_g u_g}{R(1+\Gamma)} \tag{5}$$

$$\frac{\partial}{\partial t}\left(\chi_c^d \rho_l\phi_l c_1 + \frac{\Gamma}{1+\Gamma}\rho_g\phi_g\right) = -\frac{\partial}{\partial z}\left[\left(\chi_c^d \rho_l\phi_l c_1 + \frac{\Gamma}{1+\Gamma}\rho_g\phi_g\right)v\right.$$
$$\left. + \frac{\Gamma}{1+\Gamma}\rho_g\phi_g\left(v_g - v\right)\right] - \frac{2\Gamma\rho_g\phi_g u_g}{R(1+\Gamma)} \tag{6}$$

The radially averaged momentum balance (Equation 3) gives magma velocity v as the sum of incompressible, steady, laminar Poiseuille Flow v_{visc}, and rate-dependent frictional slip v_{fric} (Rice et al., 2001) (full derivation in Wong & Segall, 2019). Flow is driven by the difference between the vertical pressure gradient $\partial p / \partial z$ and the gravitational load ρg, giving shear stress τ_R. The conduit has constant radius R. The conduit walls have depth-dependent effective normal stress $\sigma_c(z)$, which is the difference between lithostatic normal stress and hydrostatic pore pressure, $\left(\rho_{lith} - \rho_{hyd}\right)gz$, neglecting tectonic and topographic contributions. Wall friction is parameterized by the nominal coefficient f_0, rate-dependence a, and reference velocity v_r. Deep in the conduit, where η is low and σ_c is high, v_{visc} predominates and magma flows viscously. In the shallow part of the conduit, magma solidification increases η while σ_c decreases, increasing v_{fric} until frictional sliding dominates.

Continuity for solids and liquids (Equation 4) reflects the exchange of mass as liquid melt solidifies during ascent. Continuity for H_2O (Equation 5) contains both dissolved and exsolved components. In a previous study, we examined steady-state solutions to this system of equations by neglecting the derivatives of Equations 4–6 with respect to time (Wong et al., 2017). However, to study the temporal evolution of slow-

Table 1
Continued

Symbol	description
k_{wall}	Wall-rock permeability
k_{lat}	Lateral permeability
p_{ch}	Chamber pressure
p_{deep}	Pressure in deep magma source
p_{hyd}	Pore pressure in the crust
Q_c^{ex}	Carbon dioxide flux
T_{ch}	Chamber pressure evolution timescale
u_g	Lateral gas velocity
v_g	Vertical gas velocity
V_{ex}	Extruded volume (DRE)
v_{fric}	Frictional slip velocity
v_{visc}	Viscous flow velocity
β_{ch}	Chamber compressibility
β_{mag}	Magma compressibility
Γ	Mass ratio of exsolved CO_2 to H_2O
η	Mixture viscosity
η_m	Melt viscosity
η_s	Relative viscosity due to solids
ρ	Magma mixture density
ρ_g	Gas density
σ, σ_c	Normal stress (Lithostatic, effective)
τ_R	Shear stress along conduit wall
ϕ_l	Melt volume fraction
ϕ_s	Solid volume fraction
χ_c^d	Mass concentration of dissolved CO_2
χ_h^d	Mass concentration of dissolved H_2O

er dome-forming eruptions, these time derivatives become important. Transient mass changes are balanced by the flux of volatiles as well as vertical and lateral gas flow out of the conduit at gas velocities v_g and u_g respectively (e.g., Kozono & Koyaguchi, 2012; Schneider et al., 2012). The term $\Gamma = (1 - m_h)\mathcal{M}_c / (m_h \mathcal{M}_h)$ is the mass ratio of exsolved CO_2 to H_2O, where m_h is the mole fraction of water in the vapor phase and $\mathcal{M}_c, \mathcal{M}_h$ are the molar masses of CO_2 and H_2O respectively. A similar form describes continuity of CO_2 (Equation 6).

To model gas escape from the system, we apply Darcy's Law while assuming chemical and mechanical equilibrium between the gas phase and the ambient melt (Jaupart & Allègre, 1991; Kozono & Koyaguchi, 2012; Schneider et al., 2012). This implies that gas and melt pressures are the same. The gas velocities are given by

$$\left(v_g - v\right) = \frac{k_{mag}}{\eta_g}\frac{\partial p}{\partial z} \tag{7}$$

$$u_g = \frac{k_{lat}}{\eta_g}\frac{p - p_{hyd}}{2R}, \tag{8}$$

where η_g is the gas viscosity, and $p_{hyd} = \rho_{hyd}gz$ is the hydrostatic pressure. In vertical gas escape, gas flows through the magma only, thus the permeability constant in Equation 7 is the magma permeability k_{mag} modeled using the Carman-Kozeny relation,

$$k_{mag} = k_c\phi_g^3, \phi_g \geq \phi_{gc}, \tag{9}$$

where k_c is a scaling constant, ϕ_g is the gas volume fraction (porosity), and ϕ_{gc} is the percolation threshold, which is the minimum porosity to form interconnected pathways and has a typical value of ~30% (Blower, 2001; Klug & Cashman, 1996; Saar & Manga, 1999). In lateral gas escape, gas flows through both magma and the wall rock. The lateral permeability k_{lat} is a harmonic average of k_{mag} and k_{wall}, the depth-dependent crustal permeability model from Manning and Ingebritsen (1999). The pressure gradient driving lateral gas flow is approximated as the difference between magma pressure and a far-field hydrostatic pressure, over the length scale of two conduit radii (Wong & Segall, 2019).

2.1.2. Boundary and Initial Conditions

Taking into account the constitutive relations, the model solves for four field variables in the conduit at each depth and time: pressure, velocity, gas volume fraction (porosity), and mole fraction of water in the vapor phase, compiled into the vector $y(z,t) = [p, v, \phi_g, m_h](z,t)$. Other variables, such as density and viscosity, are derived from these primary variables (Table 1). The governing equations are solved using a staggered grid with a finite difference discretization (Wong & Segall, 2019). Fluxes are calculated using Quadratic Upstream Interpolation for Convective Kinematics, which is conducive for propagating information along the flow direction (Leonard, 1995). Pressure gradients are calculated using central differencing. Details on the numerical method are given in (Wong & Segall, 2019).

The governing equations consist of $4(N_z-1)$ equations, where N_z is the number of depth points. This system of equations requires four boundary conditions to be complete: pressure and volatile contents (H_2O and CO_2) in the chamber, and pressure at the top of the conduit.

At the beginning of the eruption, chamber pressure must be greater than the magma column weight to drive upward flow. As the eruption proceeds, magma outflux q_{out} causes the chamber pressure to decrease, while influx q_{in} from a deeper source may increase the chamber pressure (e.g., Segall, 2013),

$$\frac{dp_{ch}}{dt} = \frac{q_{in} - q_{out}}{\rho_0 V_0 \left(\beta_{mag} + \beta_{ch}\right)} = \frac{\Omega\left(p_{deep} - p_{ch}\right) - \pi R^2 v_{ch}}{V_0\left(\beta_{mag} + \beta_{ch}\right)},$$ (10)

where Ω is a proportionality constant linking recharge in the chamber to the magmastatic head between the chamber and a deep reservoir at constant pressure p_{deep}, v_{ch} is the velocity at the conduit base, V_0 is the initial chamber volume, while β_{mag} and β_{ch} are the magma and chamber compressibilities respectively,

$$\beta_{mag} = \frac{1}{\rho}\frac{\partial\rho}{\partial p}, \quad \beta_{ch} = \frac{1}{V}\frac{\partial V}{\partial p},$$ (11)

where ρ, p are evaluated at the center of the chamber (Anderson & Segall, 2011). Pressure at the center of the chamber is the sum of pressure at the conduit inlet and magmastatic head from the chamber top to center. To calculate magma compressibility, we simultaneously solve for density (using Equation 1) and chamber center pressure given the conduit length and chamber depth, volume, and aspect ratio. We then use finite differences to approximate $\partial\rho / \partial p$. Chamber compressibility is estimated from the numerical results for different ellipsoidal chamber shapes (Amoruso & Crescentini, 2009).

Scaling analysis of Equation 10 gives the timescale of chamber pressure evolution depending on recharge rate as

or
$$T_{ch}^{(1)} = \frac{V_0\left(\beta_{mag} + \beta_{ch}\right)}{\Omega}\left(\text{fast recharge}\right),$$
$$T_{ch}^{(2)} = \frac{p_{ch}^0 V_0\left(\beta_{mag} + \beta_{ch}\right)}{\pi R^2 v_{ch}^0}\left(\text{slow recharge}\right).$$ (12)

Comparing T_{ch} with the ascent timescale (L/v) reveals when transient terms are significant. If the chamber pressure evolution timescale is long relative to the ascent timescale, the time-dependent model should approximate steady-state solutions evaluated at the identical chamber pressure (Wong & Segall, 2019). This could occur, for example, if the chamber volume is large (>1,000 km³). On the other hand, if the chamber pressure evolution and ascent timescales are comparable, full time-dependent solutions are needed to model conduit flow.

Other boundary conditions are the H_2O and CO_2 mass concentrations in the chamber χ_h^{ch}, χ_c^{ch}. Using the solubility equations, the volatiles are separated into dissolved and exsolved components to determine the gas volume fraction ϕ_g and mole fraction of water m_h at the base of the conduit.

Finally, the pressure at the conduit exit is assumed to be atmospheric pressure. Note that dome growth may exert a backpressure at the conduit outlet as in Anderson and Segall (2013), however here we maintain a constant exit pressure as a simple assumption.

We initialize the model with the steady-state solution given specified boundary conditions at $t = 0$ using the code from Wong et al. (2017). Natural eruptions clearly do not start from steady-state, and future work is needed to derive more realistic eruption onsets that simulate acceleration of partially solidified conduit magma leftover from lava dome eruptions in the 1980s.

2.1.3. Model Parameters and Prior Bounds

To solve each forward model, we specify magma chamber properties (aspect ratio, volume), conduit geometry (length, radius), material properties (magma permeability scale, conduit wall friction), and conduit base boundary conditions (initial pressure, volatile contents). In this study, we set the recharge rate Ω to zero because the extruded volume time series appears to flatten out at the end of the eruption, suggesting

Table 2
Model Parameters With Their Prior Bounds, Best Fit Values From the Neighborhood Search, as Well as the Median Model and 90% Credible Interval From the Neighborhood Appraisal

| Symbol	Description	Prior bounds	Best fit from search	Median model	90% credible interval
	Chamber properties				
α	Aspect ratio (width/height)	0.05–1	0.30	0.36	0.13–0.55
V_0	Volume (km^3)	10–500	130	136	64–256
Ω	Recharge rate ($m^3\ day^{-1}\ Pa^{-1}$)	0 (fixed)	-	-	-
	Conduit geometry				
L	Length (km)	2–8	4.6	4.8	3.0–5.8
R	Radius (m)	10–100	21	22	12–36
	Material properties				
k_c	Magma permeability scale (m^2)	$10^{-20}-10^{-10}$	$10^{-13.5}$	$10^{-13.5}$	$10^{-14.7}-10^{-12.1}$
ϕ_{gc}	Percolation threshold	0.2–0.4	0.25	0.25	0.21–0.28
f_0	Nominal coefficient of friction	0.01–0.8	$10^{-1.7}$	$10^{-1.7}$	$10^{-1.9}-10^{-1.3}$
a	Rate-dependence of friction	$10^{-3}-10^{-1}$	$10^{-2.7}$	$10^{-2.8}$	$10^{-3.0}-10^{-2.4}$
	Conduit base boundary conditions				
Δp_0	Excess pressure at $t = 0$ (MPa)	5–50	19	19	12–26
χ_h^{ch}	Total water content (wt%)	3–7	5.6	5.7	5.0–6.4
χ_c^{ch}	Total carbon dioxide content (ppm)	100–5,000	2,900	2,800	1,600–3,900

that there is no recharge. Previous inversions also suggest that syn-eruptive recharge is minor (Anderson & Segall, 2013). The chamber centroid depth is uniquely determined from the chamber volume, aspect ratio, and conduit length. For a consistent description of the initial conduit base pressure for different conduit lengths, the total pressure at the conduit base p_{ch} is defined in terms of an excess pressure Δp_0 at $t = 0$,

$$p_{ch}(t = 0) = p_{atm} + \rho_l gL + \Delta p_0, \tag{13}$$

where p_{atm} is the pressure at the top of the conduit and ρ_l is the melt phase density. The excess pressure Δp_0 is defined for consistency and is not the actual overpressure in the chamber which depends on the actual phase composition in the conduit, which we do not know *a priori*. We choose a wide range for the model parameter prior bounds to minimize the influence of prior assumptions on the posterior probabilities (Table 2).

2.2. Data From the 2004–2008 Mount St. Helens Eruption

The 2004–2008 Mount St. Helens eruption began with swarms of shallow volcano-tectonic earthquakes on September 23, 2004 that culminated in a series of explosions starting on October 1, 2004 (Moran et al., 2008; Scott et al., 2008). These explosions gave way to lava extrusion under the crater glacier, forming a large welt on the south side of the 1980s lava dome (Dzurisin et al., 2015; Scott et al., 2008; Vallance et al., 2008). The new lava eventually broke through the glacier and was first seen on October 11, 2004. Thereafter, a series of lava spines, some of which resembled "whalebacks," were extruded on the crater floor. Extrusion was accompanied by tilt cycles (Anderson et al., 2010; Vallance et al., 2008) and repeated low-frequency and hybrid "drumbeat" earthquakes that were suggested to be caused by stick-slip motion of a solid plug ascending through the conduit (Iverson, 2008; Moran et al., 2008). After 3.3 years, eruptive activity waned and finally ended in January 2008 (Dzurisin et al., 2015).
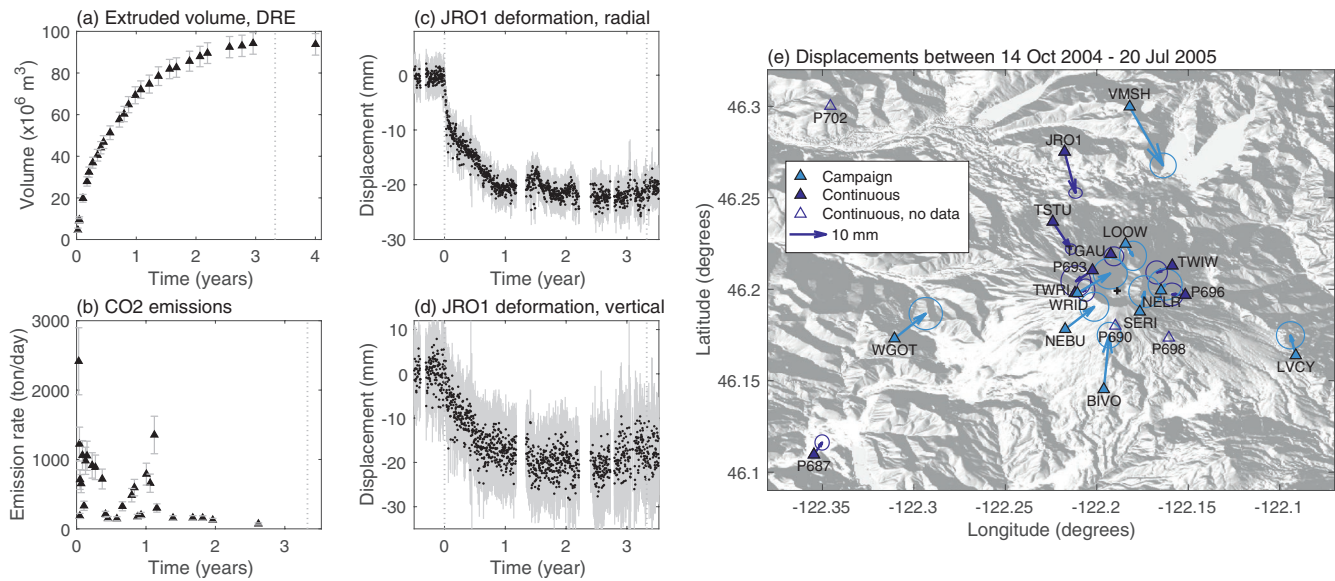
Figure 2. Data sets from the 2004–2008 Mount St. Helens eruption used in this study: (a) Dense rock equivalent (DRE) time series of extruded volume. (b) Carbon dioxide emission rates. (c and d) Radial and vertical deformation at 13 continuous Global Positioning System stations were used, here showing, as an example, JRO1, the only nearby station in operation at the eruption onset. Vertical dotted lines indicate the eruption start and end. (e) Map view of stations within 20 km of the volcano shown with displacements between two campaigns during the eruption (14 October 2004–20 July 2005). Another two stations (KELS and P421) are outside this map view. Light blue filled triangles are campaign stations, dark blue filled triangles are continuous stations in operation during this period, and dark blue open triangles are continuous stations that started operation after 14 October 2004. Black cross denotes the center of the crater.

During the eruption, a wide variety of data was collected. Three time series data sets were chosen to compare with model predictions: (1) extruded volume which indicates the evolution of exit velocity, (2) gas emissions which inform us about volatile content and permeability, and (3) ground deformation which reflects pressure change and geometry of the magma reservoir. We also include constraints on the porosity of magma exiting the conduit.

2.2.1. Extruded Volume

Differential Digital Elevation Models using aerial photogrammetry tracked the growth of the lava dome in the crater (Dzurisin et al., 2015; Schilling et al., 2008) (Figure 2a). In the initial few weeks of the eruption, lava was extruded beneath the crater glacier, precluding direct observation of dome growth. Deformation of the glacier surface showed a welt of approximately 10 ± 1 million m^3 by October 11, 2004. After that, lava broke the surface of the glacier and direct observations of the lava dome growth became possible to generate the widely used time series of dome volume change. The total extruded volume reached a maximum of 94.2 million m^3. Uncertainties in these volume estimates are ~4%. Posteruption volume decline is attributed to dome compaction. From this data, we remove an estimated dome porosity of 10% to obtain the dense rock equivalent (DRE) volume (Cashman et al., 2008; Smith et al., 2011).

From the model predictions, we calculate the DRE extruded volume from the extrusion rate by excluding the gas volume fraction and integrating over time (Anderson & Segall, 2011),

$$V_{ex}(t) = \pi R^2 \int_0^t v(z=0,t)\left[1 - \phi_g(z=0,t)\right]dt, \tag{14}$$

We compare the predicted and observed extruded volume time series to assess model fit. We additionally impose a constraint that the increase in extruded volume over the final two measurements, recorded at 3.0 and 4.0 years after the eruption start, is small (i.e., less than 4×10^6 m^3, the measurement error) to ensure that the final extrusion flux is approximately zero.

2.2.2. Carbon Dioxide Emissions

During the eruption, emissions of carbon dioxide generally decayed with time (Figure 2b). These data, along with measurements of sulfur dioxide and hydrogen sulfide, were collected via aircraft sampling of the vapor plume (Gerlach et al., 2008). Gases escaping both vertically through the conduit and laterally through the wall rocks may be observed at the surface. However, in calculating the gas flux at the surface, we approximate that all CO_2 in the plug escaped vertically. Laboratory measurements of permeability indicate that vertical permeability is much higher than lateral permeability (Gaunt et al., 2014). In addition, we would expect a time lag in gas emissions if lateral gas percolation was important. This delay was not observed: emissions decayed below the detection threshold well before the end of the eruption. Model predictions thus serve as an upper bound on vertical gas escape. We calculate the carbon dioxide emissions as

$$Q_c^{ex}(t) = \pi R^2 \frac{\Gamma}{1 + \Gamma} \rho_g \phi_g \left(v_g - v \right) \Big|_{z=0}, \tag{15}$$

where all variables are evaluated at the surface. Note that gas is also transported within pores in the magma traveling at velocity v, however, this contribution is small since v is much smaller than $(v_g - v)$ at the surface.

2.2.3. Ground Deformation From Global Positioning Stations

The eruption was monitored by a network of continuous and campaign Global Positioning System (GPS) stations around the volcano (Figures 2c–2e). Most of these stations were installed after the eruption began. Only one station, JRO1 at the Johnston Ridge Observatory, captured the eruption onset, which was characterized by rapid deflationary motion of about 10 mm in 2 weeks (Anderson & Segall, 2013; Lisowski et al., 2008).

To obtain the volcanic deformation signal, we downloaded and processed position time series from continuous GPS stations in the USGS Pacific Northwest Network, focusing on stations within 100 km of Mount St. Helens. Stations on Mount Rainier were omitted because of strong measurement drift due to snow. The region around Mount St. Helens experiences long-term deformation due to convergence of the North American and Juan de Fuca plates, slow slip events, seasonal fluctuations, and volcano-related deformation. We first identify slow slip time intervals between 1999 and 2020 using the relative strength index (Crowell et al., 2016) on the 36 stations located between 20 and 100 km of the volcano. Stations within 20 km were not used to identify slow slip time intervals because of strong seasonal and volcanic deformation signals. A slow slip event must be identified by at least two stations to be accepted. Next, we simultaneously estimated tectonic deformation rates, slow slip offsets, sinusoidal seasonal effects, and amplitudes for power law noise (white, flicker, and random walk) using the Maximum Likelihood Estimation (MLE) approach (Langbein, 2004; Mao et al., 1999; Williams, 2008) on the posteruption position time series (2012–2020) which has no discernible volcanic deformation. We assume that tectonic deformation, seasonal variability, and noise amplitudes are the same before and after 2012. We remove the tectonic deformation and seasonal signal from the whole time series and apply the noise amplitudes to the covariance matrix of syn-eruptive measurements. Offsets due to slow slip events and antenna maintenance before 2012 were removed by taking averages before and after the offset. The result is the deformation due to volcanic activity.

Of the GPS stations within 100 km of Mount St. Helens, 21 are within 60 km of the volcano and recorded displacements during the eruption period. Eight of these 21 continuous stations only recorded the latter half of the eruption when deformation was limited and were thus excluded from the inversions. For the remaining 13 stations, the covariance matrix for the deformation time series was modeled using the uncertainties in the tectonic velocity and slow slip offset estimates, and the variance of the noise processes obtained in the MLE. Note that data during slow slip events were removed, causing gaps in the time series, because we do not model time-dependent slow slip deformation.

Additional campaign GPS measurements from nine stations between October 14, 2004 and July 20, 2005 were incorporated in the analysis. This time period spans 0.05–0.8 years after eruption onset. Based on the continuous station data, this period encapsulates a large proportion of the total syn-eruptive deformation. These campaign measurements can therefore provide additional constraints on chamber geometry and

depth. Tectonic velocities at the continuous GPS stations were linearly interpolated (i.e., assuming constant strain and rotation rate) to remove tectonic velocities at the campaign GPS stations. Slow slip offsets and seasonal fluctuations were ignored due to lack of constraints, which may bias the campaign displacements. In particular, vertical deformation at the near-vent, high elevation stations had high errors, presumably due to snow on the antennas.

From the model-predicted pressure decay time series, we calculate radial displacements using the expressions of Yang et al. (1988) for prolate spheroidal chambers. We do not consider the effect of conduit tractions on surface displacements, because the GPS stations are far from the vent relative to the plug length.

2.2.4. Additional Constraint on Magma Porosity

As an additional inversion constraint, we included data on the porosity of dome lava specimens collected by helicopter (Pallister et al., 2008; Thornber et al., 2008). These specimens consist of dense, light-gray dacite with porosities below 10% and vesicular, dark gray to red dacite with porosities of 25%–40% (Cashman et al., 2008). One helium pycnometer measurement indicated a connected porosity of 30.4% (Cashman et al., 2008). Five intact samples with no deformation textures showed porosity declining from 19.7% to 10.3% after 2 years (Smith et al., 2011). Applying the porosity time series from Smith et al. (2011) directly to the inversion is challenging because of the small number of samples and the fact that they consist of intact, centimeter to meter scale samples which may not be representative of the average porosity across the tens-of-meter scale conduit. Therefore, we opt for a simple constraint that admits only models whose predicted porosity time series is entirely less than the maximum observed porosity of 40%.

2.3. Inversions Using the Neighborhood Algorithm

We apply the neighborhood algorithm (Sambridge, 1999b, 1999a) to estimate critical properties of the Mount St. Helens plumbing system. Previous studies have applied this algorithm to volcano deformation to determine the location and volume change of magma chambers, as well as to model dike geometry from InSAR data (e.g., Fukushima et al., 2005; Pritchard & Simons, 2002). The neighborhood algorithm consists of two stages: (1) the model space search and (2) the ensemble appraisal.

2.3.1. Searching the Model Space

Stage 1 generates an ensemble of models by searching the model space to find models that have high posterior probabilities (Sambridge, 1999b). This stage is akin to an adaptive grid search. In this section, we first define the posterior probability and then describe the search algorithm.

The 12 model parameters (e.g., chamber aspect ratio, chamber volume, etc.) are compiled in the vector $\mathbf{m}$, and the data (extruded volume, deformation, gas emissions, and porosity) are compiled into the vector $\mathbf{d}$. The posterior probability $p(\mathbf{m}|\mathbf{d})$ of each model given the observed data is

$$p(\mathbf{m}|\mathbf{d}) \propto L(\mathbf{d}|\mathbf{m}) p(\mathbf{m}) \tag{16}$$

where $L(\mathbf{d}|\mathbf{m})$ is the data likelihood, which measures the fit between observed and predicted data, and $p(\mathbf{m})$ is the prior probability distribution, which encodes some information on the parameter known before the analysis. The posterior probability is analogous to an update to our prior understanding once we have included information from the observations. In this study, we assume uniform priors on the model parameters, however this inversion scheme can be easily adjusted to incorporate other priors. Uniform priors have constant $p(\mathbf{m})$ while $\mathbf{m}$ is within predefined bounds. The data likelihood is

$$L(\mathbf{d}|\mathbf{m}) \propto \exp\left[-\frac{1}{2}\frac{1}{\sum_k w_k}\Phi\right], \tag{17}$$
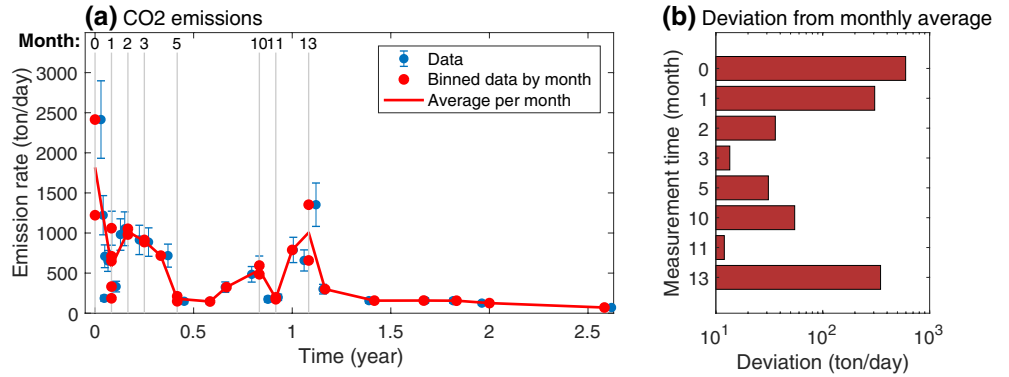
Figure 3. Determining the weight for the CO_2 emissions time series. (a) Observed emissions (blue dots with error bars) and binned by month (red dots). Red line tracks the average for each month. Months with more than one observation are indicated at the top of the axis. (b) Root-mean-square of deviations of observed CO_2 emissions from the monthly average for the 8 months that had multiple observations.

$$where\ \Phi = \sum_k \left[w_k \left(d_k - \hat{d}_k \right)^T C_k^{-1} \left(d_k - \hat{d}_k \right) \right],$$

(18)

where k denotes the data set (extruded volume, continuous GPS positions, campaign GPS displacements, CO_2 emissions, porosity constraint) and Φ is the joint misfit to the data. For the kth data set, w_k is the weight, d_k are the observed data, $\hat{d}_k$ are the predicted data, and C_k is the covariance matrix.

The simplest joint misfit is obtained by assigning equal weights ($w_k = 1$) for all k data sets. However, initial tests show that this approach does not find well-fitting solutions because of the high scatter in the CO_2 emissions. This scatter arises from unmodeled processes (e.g., crack propagation in the plug that allows sudden release of gases) or measurement errors (e.g., wind dispersal of emissions) that cannot be captured by the current physics-based model, which can only predict smoothly decaying solutions. Therefore, we reduce the weight of the CO_2 emissions w_{CO2} to prevent the misfit to the CO_2 emissions from dominating the total misfit. To determine w_{CO2}, we bin the emissions into months and examine the variability among measurements in the same month (Figure 3). During the 2.6-year observation duration, 8 months had more than one observation (months 0, 1, 2, 3, 5, 10, 11, 13). In these 8 months, the root-mean-square deviation from the monthly average ranged from 12 to 597 ton/day. Normalizing the high estimate of 597 ton/day by the median measurement error of 97 ton/day gives a scale factor of 6.15. Therefore we assign w_{CO2} as the reciprocal of the square of this scale factor to get units of variance, giving $w_{CO2} = 1/(6.15^2) = 0.0264$. Weights to all other data sets were assigned as 1.

The neighborhood search algorithm is as follows: first, N_s model parameter combinations are randomly chosen to run the forward model and evaluate the joint misfit (Equation 18). The forward model evaluations can be run in parallel. From this set of models, the best fitting N_r models, where $N_r \leq N_s$, are selected for the next iteration. This is equivalent to models with the highest posterior probability within the prior bounds. In the next iteration, a new set of N_s/N_r models is generated in the neighborhood of each selected model. As an example, if $N_s = 200$, $N_r = 100$, the 100 best fitting models are chosen at this stage, and two new points are generated in the neighborhood of each of these 100 models to generate a total of 200 new points. The "neighborhood" is defined using Voronoi cells, where the cell boundary is the midpoint of two models. Sambridge (1999b) provides an efficient method to calculate these cell boundaries. The misfits of each of these new models are then evaluated, and the process of selecting well-fitting cells and generating new models and misfits is repeated until the minimum misfit approaches a constant.
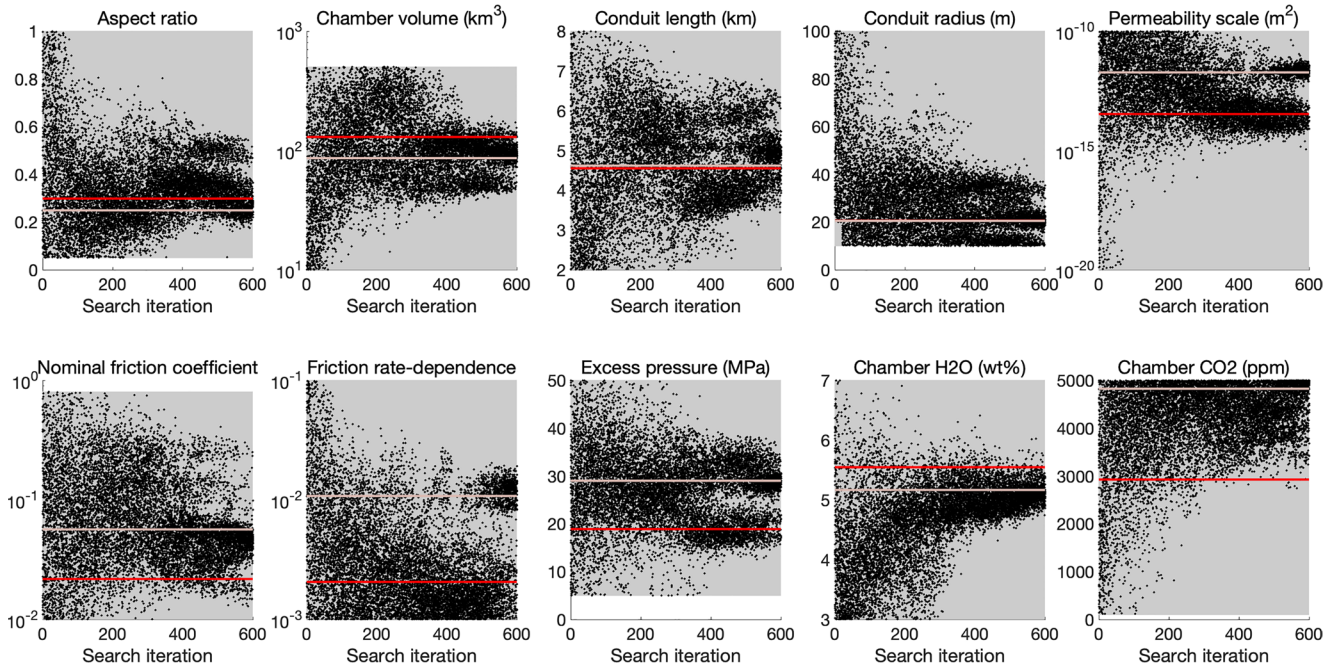
Figure 4. Model parameters at each neighborhood search iteration. Inversion bounds for model parameters are delineated by the gray rectangle (in some cases equivalent to the limits of the vertical axis). Red line marks the best fit model. Pink line marks one model with nonsmooth solutions.

The neighborhood search is simple to implement and only requires two tuning parameters N_s, N_r which influence the effectiveness of the model space search. Large N_s, N_r produce a more exploratory search; small N_s, N_r improve the algorithm's capability as an optimizer although it may become susceptible to local minima.

2.3.2. Appraising the Ensemble of Models

Stage 2 resamples the ensemble of models generated in Stage 1 using a Gibbs Sampler to generate PDFs of the model parameters (Sambridge, 1999a). Within the neighborhood of each model, the posterior probability $p(\mathbf{m}|\mathbf{d})$ is assumed to be constant, so that no new forward model evaluations are required.

The Gibbs Sampler procedure is as follows: starting from a high probability model, a random step is taken along the first parameter axis according to the posterior probability conditional on fixed values for the other 11 parameters $p(m_1|m_2, m_3,...m_{12}, \mathbf{d})$, where m_i are the model parameter values of the high probability model. This probability is derived from the posterior probability $p(\mathbf{m}|\mathbf{d})$. To generate this random step, we follow Sambridge (1999a) and use the rejection method: first, a uniform random deviate m_1^{prop} is generated within the specified model parameter bounds. The proposed step is then compared with the maximum probability along that axis and another uniform random deviate r on the interval (0,1). The proposed step is accepted if

$$\log r \le \log p\left(m_1^{prop} \mid m_2, m_3,...m_{12}, \mathbf{d}\right) - \max\left[\log p\left(m_1 \mid m_2, m_3,...m_{12}, \mathbf{d}\right)\right].\tag{19}$$

If m_1^{prop} is rejected, a new uniform random deviate m_1^{prop} is generated and compared to r until a step is accepted. The procedure then moves to the second parameter axis and takes a random step according to the probability $p(m_2|m_1, m_3,...m_{12}, \mathbf{d})$, and so on for each of the 12 parameter axes, and then on subsequent samples. The rejection method should be implemented with log probabilities as above to avoid numerical underflow issues.

Two input parameters are needed for the Gibbs sampler: the length of each Gibbs sampling chain and the number of chains. We test different values for these two parameters until the PDFs converge. For
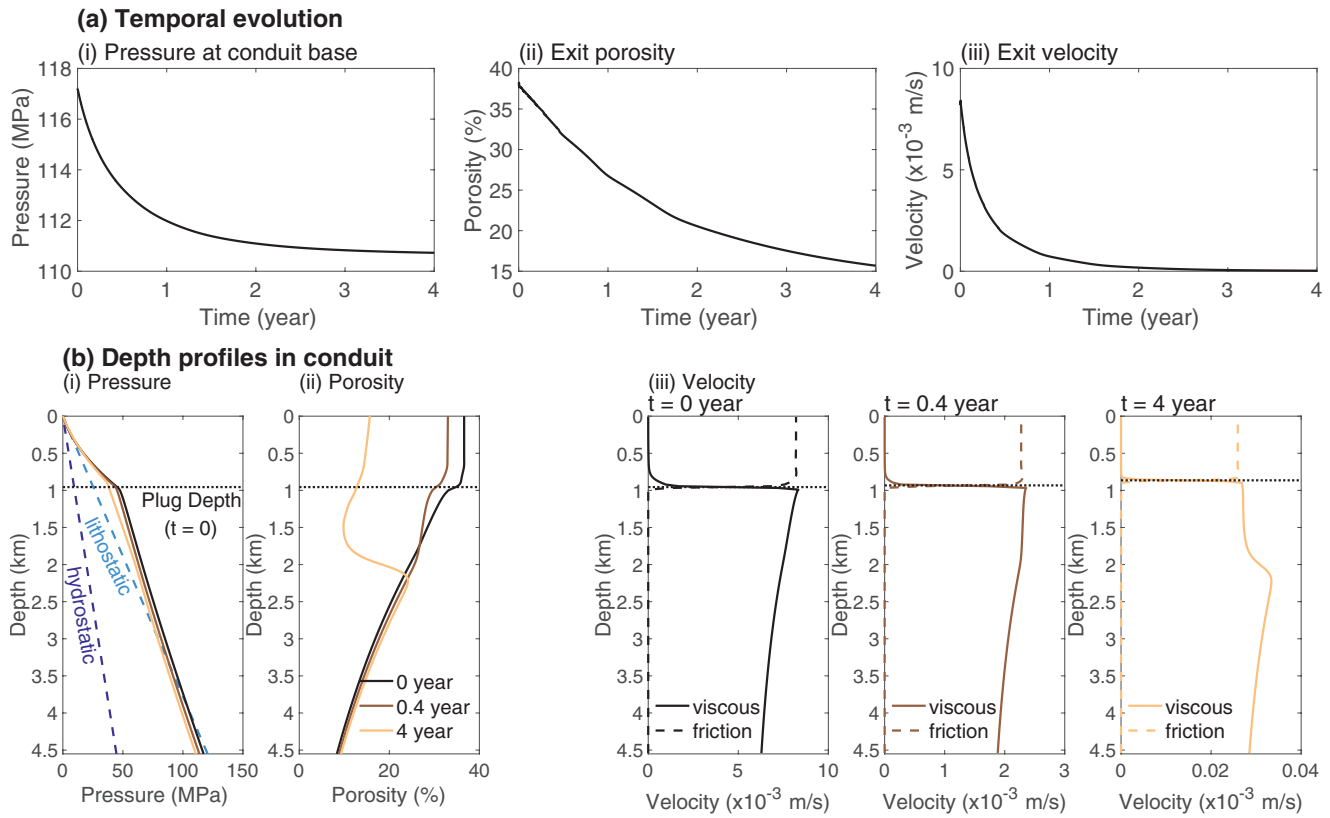
Figure 5. Solution of the model with the highest posterior probability in the ensemble. (a) Temporal evolution of (i) chamber pressure, (ii) exit porosity, and (iii) exit velocity. (b) Depth profiles of (i) pressure, with assumed hydrostatic and lithostatic pressure profiles are given in blue dashed lines, (ii) porosity, and (iii) velocity at three times (0, 0.4, and 4 years; note different horizontal scales). The plug depth at $t = 0$ is indicated in the black dotted lines.

this study, we found that the chain length should be at least 2000 and the number of chains should be at least 50.

3. Results

3.1. The Model Parameter Space

For Stage 1 of the neighborhood algorithm, we run the algorithm with $N_s = N_r = 200$ for 600 iterations, which was sufficient for model parameters to converge and for maximum model likelihoods to reach a stable value (Figure 4). Parameters for the maximum likelihood model lie well within the prescribed bounds. After 20 iterations, we reduced the lower bound of conduit radius from 20 m to 10 m as the best fit model appeared to be very close to 20 m. Chamber aspect ratio and volume appear to converge after about 400 iterations. Other parameters converge more slowly, eventually reaching a stable maximum likelihood model (red line, parameters in Table 2). During the search, the algorithm also explored a secondary, local maximum (pink line in Figure 4). On closer inspection, we observe that these models have nonsmooth solutions caused by a slight numerical instability at the percolation threshold. Smoothing the percolation threshold transition removes this instability, but the predicted data for these models produce poor fits to the observations. In particular, these solutions fail to satisfy the zero flux condition at the end of the eruption. Therefore, we reject these nonsmooth solutions as unphysical.

From the search step, we find a model that maximizes the posterior probability (parameters given in Table 2). The temporal evolution and depth profiles of solution variables are shown in Figure 5. At the beginning of the eruption, pressure at the conduit base is 117.2 MPa. This is just slightly below lithostatic pressure at the
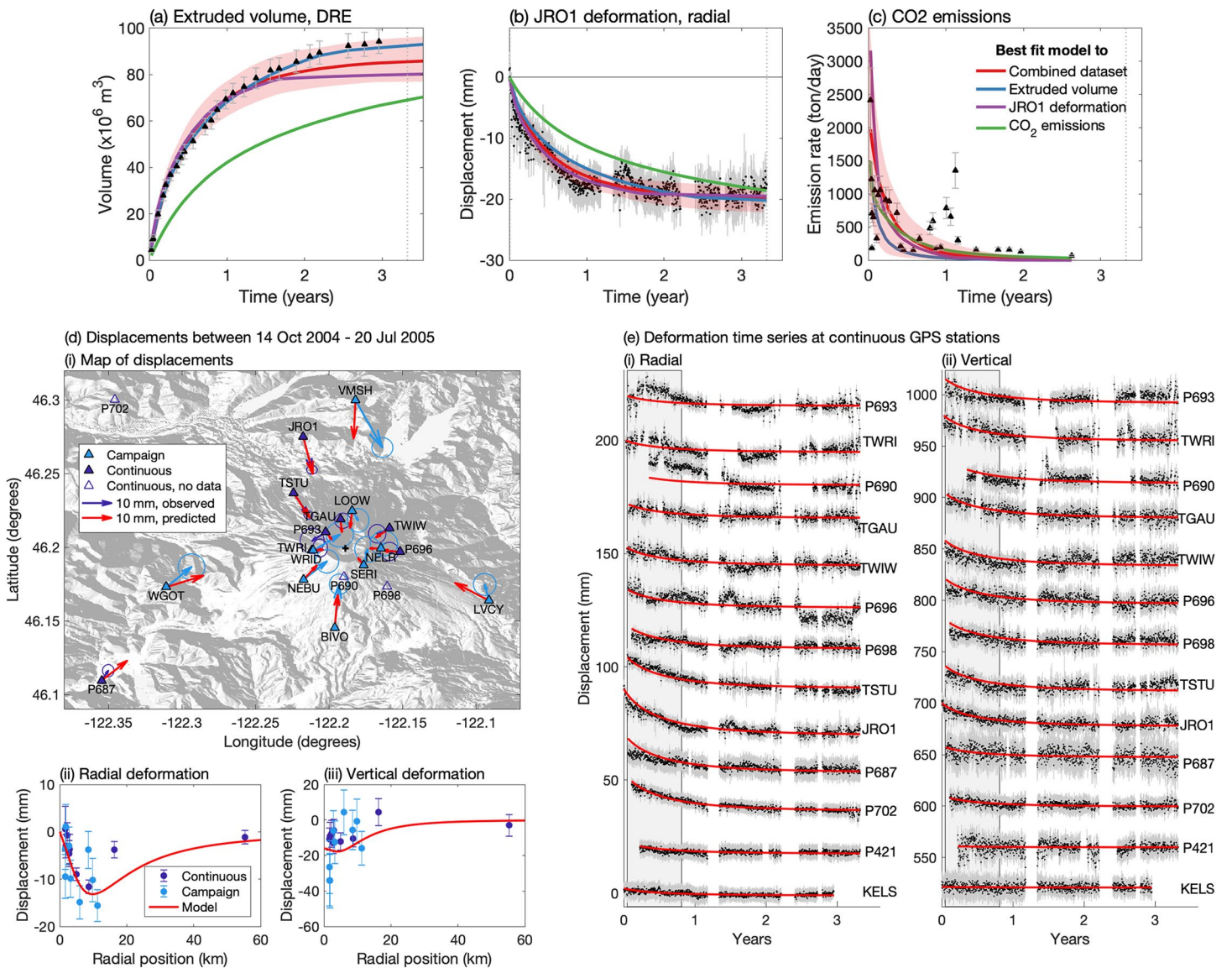
Figure 6. Best fit model to the combined data set (red line) compared to observations. (a) Extruded volume, (b) JRO1 radial displacement, and (c) CO_2 emissions time series. For (a–c), the range of the models accepted in the appraisal step (pink envelope), as well as the best fit models to individual data sets are also shown. Vertical gray dotted lines indicate the eruption end. (d) Predicted displacements from the best fit model to the combined data set, showing the (i) map, (ii) radial displacements, and (iii) vertical displacements as functions of radial distance from the crater. (e) Predicted radial and vertical deformation time series at the continuous Global Positioning System stations, ordered by closest (P693) to furthest (KELS) from the crater. Vertical gray rectangle indicates the time period of the two campaigns. Gaps in the time series occur during slow slip events.

same depth. Pressure decays to 110.8 MPa at the eruption end time of 3.3 years. We assume no recharge into the chamber. Decreasing driving pressure decreases exit velocity by more than two orders of magnitude, while the longer ascent time allows more gas to escape, causing the exit porosity to drop. This can be seen in the depth profiles of porosity (Figure 5b(ii)), where porosity of the $t = 4$ years decreases dramatically above the percolation threshold at 2.2 km depth. Exit porosity during whole simulation is below 40% as required by the porosity constraint (Figure 5a(ii)).

The fit to observations is calculated from the solution variables (Figure 6). Predicted extruded volume from the best fit model to the combined data set (red line) matches early observations well, but the final extruded volume allowed to be slightly lower than observations because the measurement error increases with volume. Similarly, the models accepted in the appraisal step (pink envelope) closely follow early volume estimates but show a wider range of final extruded volume. The predicted JRO1 radial displacement follows the observations well. Due to the lower weight applied to the CO_2 emissions time series, the pink envelope spans a wide range, broadly capturing the decreasing trend and range of values.

Predicted radial displacements between October 14, 2004 and July 20, 2005 largely agree with the observations, particularly at the continuous GPS stations (Figure 6d(ii)). Radial displacements at the campaign stations are noisier but follow the same general trend. Fits to vertical deformation during this time are poorer. Campaign stations WRID, NELR, and SERI experienced large vertical displacements (light blue points between −20 and −40 mm in Figure 6d(iii)) that are likely caused by seasonal effects such as snow accumulation because these stations are at high elevation. The rest of the vertical deformation data suggest that the maximum displacement should be offset from the crater center (where radial distance is zero), supporting a prolate ellipsoid model for the chamber (Yang et al., 1988). This same model also fits the deformation time series at the continuous GPS stations.

Compared to the best fit models to individual data sets, the best fit model to the combined data set cannot match each observation as well (Figures 6a–6c). Some penalization of fit is needed. For example, the best fit model to the JRO1 deformation (purple line) captures the initial rapid deflation which flattens out after 1 year. However, this trend yields poor fits to the observed extruded volume both in magnitude and temporal trend. In order to simultaneously fit the deformation and extruded volume time series, the search finds models that have slightly poorer fit to the initial rapid deflation at JRO1. Similarly, the best fit model to the extruded volume time series (blue line) has a poorer fit to the initial rapid deflation. Compared to the best fit model to the CO_2 emissions (green line) which produces a significantly poorer fit to the other data sets, the best fit model to the combined data set has a distinctively different trend.

3.2. Posterior Probabilities of Model Parameters

We appraise the ensemble of models to generate posterior PDFs of the model parameters by converting misfits to likelihoods (Equation 17, Figure 7). For comparison, we also calculate the likelihoods given only extruded volume, only deformation, and the combination of extruded volume and deformation from the ensemble, and appraise the result. For these appraisals, we also apply the constraints on dome porosity and zero final extrusion flux.

In general, when more data sets are used, the marginal posterior PDFs show tighter constraints on the model parameters as expected. The extruded volume time series constrains the chamber volume, conduit radius, nominal friction coefficient, excess pressure, magma permeability scale, and total volatile contents (Figure 7a). Total extruded volume scales as $\left(\beta_{\mathrm{mag}} + \beta_{\mathrm{ch}}\right)\Delta p_{\mathrm{ch}}V_0$ (Segall, 2013) and therefore can offer constraints on chamber volume given estimates of compressibility which depend on the exsolved volatile content. The extrusion rate can help to constrain the exsolved volatile content, as a higher exsolved volatile content would decrease bulk density and enable faster magma ascent. However, this relationship may not be unique as the extrusion rate is also affected by the driving pressure, rate of gas escape, and frictional resistance.

Deformation data alone improve constraints on chamber properties (aspect ratio, volume, conduit length which controls chamber centroid depth, excess pressure), but volatile content and frictional properties are poorly constrained (Figure 7b). When extruded volume and deformation are jointly applied, the distributions on all the model parameters except the frictional properties become narrower (Figure 7c). This estimation is enhanced by inclusion of CO_2 emissions data in the appraisal. Naturally, the distribution on chamber CO_2 content is tighter and slightly lower than estimated in the other three appraisals. This lower volatile content may explain the slightly lower nominal friction coefficient: a decrease in magma buoyancy requires a corresponding decrease in flow resistance.
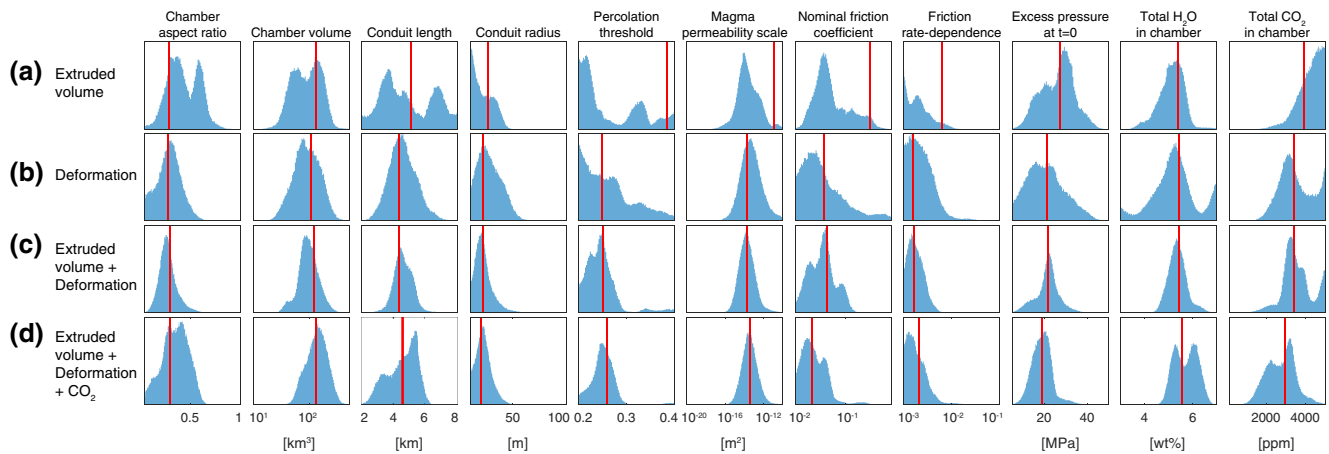
Figure 7. Marginal posterior probability density functions of the model parameters when the appraisal is constrained by different data sets: (a) uses extruded volume time series only, (b) uses continuous and campaign GPS data only, (c) uses extruded volume, continuous and campaign GPS data, while (d) uses all data sets. Limits of the horizontal axis correspond to the bounds of the uniform prior. Vertical red lines denote the highest likelihood models for each appraisal.

In all four ensemble appraisals, the magma permeability scale is well constrained to be above 10^{-16} m^2, with all four distributions having approximately similar widths. This indicates that dome porosity data, which are common to all four appraisals, are the main control on magma permeability scale. In order for the dome porosity to remain under 40%, magma permeability has to be high enough to allow volatiles to escape from the conduit.

In the following sections, we analyze the results of the appraisal by looking at subsets of parameters. Any quoted ranges of parameter values are the 90% credible intervals of the posterior PDF.
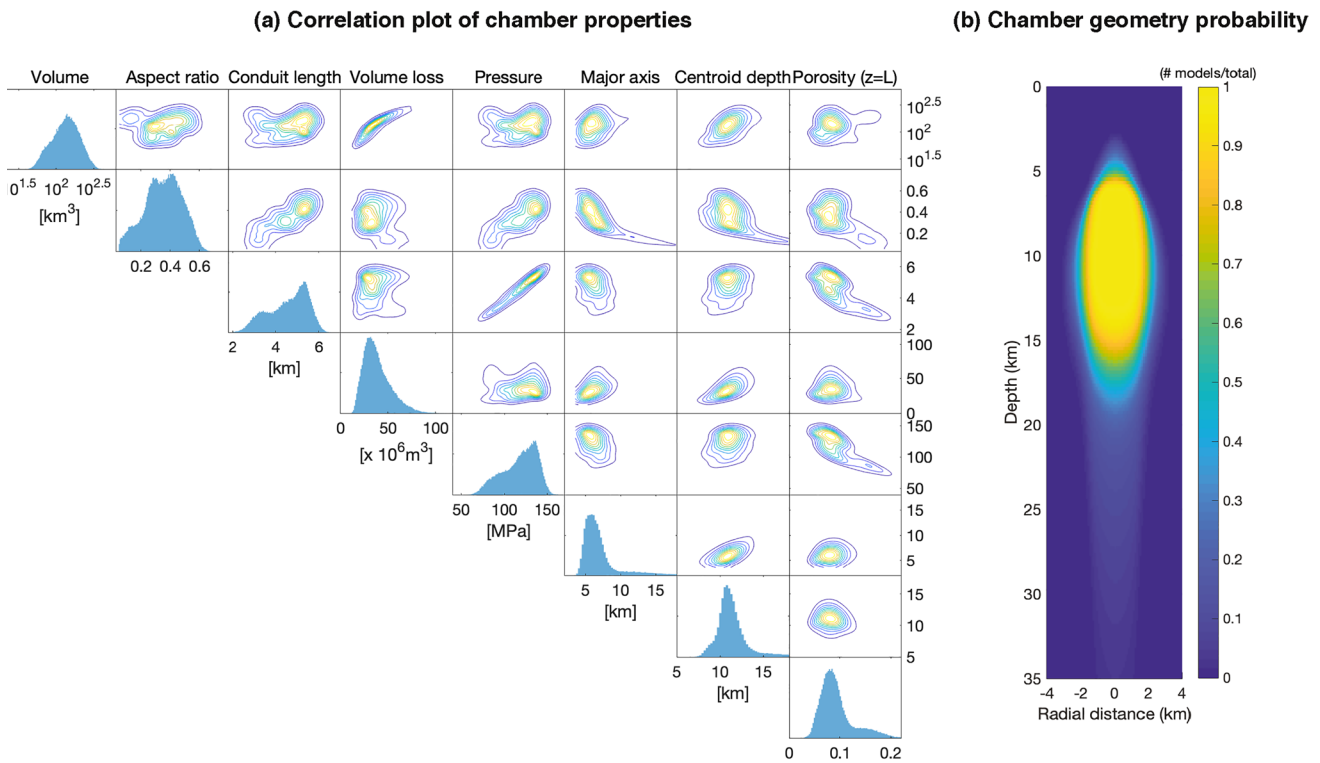
3.2.1. Chamber Properties

The preferred chamber volume lies between 64–256 km^3 (Figure 8a), well below the threshold for the chamber evolution timescale to be comparable to the ascent timescale. This implies that steady-state solutions are poor approximations to the temporal evolution of the system, rather requiring the full time-dependent governing equations (Wong & Segall, 2019). The data prefer an elongate chamber with an aspect ratio (width/height) of 0.13–0.55 with its top (equivalent to conduit length) located at 2.9–5.8 km depth. The chamber centroid is located at 9–17 km depth with the semimajor axis estimated as 4.6–14.0 km. These parameters indicate that the chamber likely lies between 5–20 km depth and spans about 2 km in width (Figure 8b).

The chamber geometry parameters are highly correlated. Aspect ratio exhibits a negative correlation with the semimajor axis because of how they affect the chamber volume: a more elongate chamber requires a longer axis to occupy the same volume. A more elongate chamber also has to be located deeper. Volume loss in the chamber, which ranges between 20 and 66×10^6 m^3, exhibits a positive correlation with volume and centroid depth. Pressure at the conduit base ranges from 81–144 MPa and is highly correlated with conduit length to ensure that magma can be pushed out of the conduit at a similar velocity. This corresponds to 13–55 MPa over magmastatic pressure (weight of magma column) needed to overcome viscous losses and frictional resistance. Porosity at the conduit base not only depends on the total water content (not shown), but also the conduit length and pressure at the base of the conduit.

3.2.2. Volatiles and Permeability

Volatile contents in the chamber are well-constrained in the appraisal (Figures 9a and 9b). Total H$_2$O contents of 5.0–6.4 wt% and CO$_2$ contents of 1,600–3,900 ppm are preferred. These volatile contents are partitioned into dissolved and exsolved components. Dissolved H$_2$O encompasses the relatively common 3.3–4.6 wt% for arc magmas (Plank et al., 2013), while dissolved CO$_2$ is estimated to be 22–100 ppm. Together, these imply a substantial exsolved phase occupying 5%–16% volume fraction at the base of the

Figure 8. Chamber properties constrained in the appraisal that considers the likelihood of all the data sets. (a) Correlation plot of the chamber properties. Volume, aspect ratio, and conduit length are directly estimated, while the rest are dependent variables. Pressure and porosity are for the top of the chamber. (b) 2D slice of the crust showing the probability of finding a chamber at a certain radial distance and depth below the vent of Mount St. Helens. Colors indicate the number of models relative to the total.
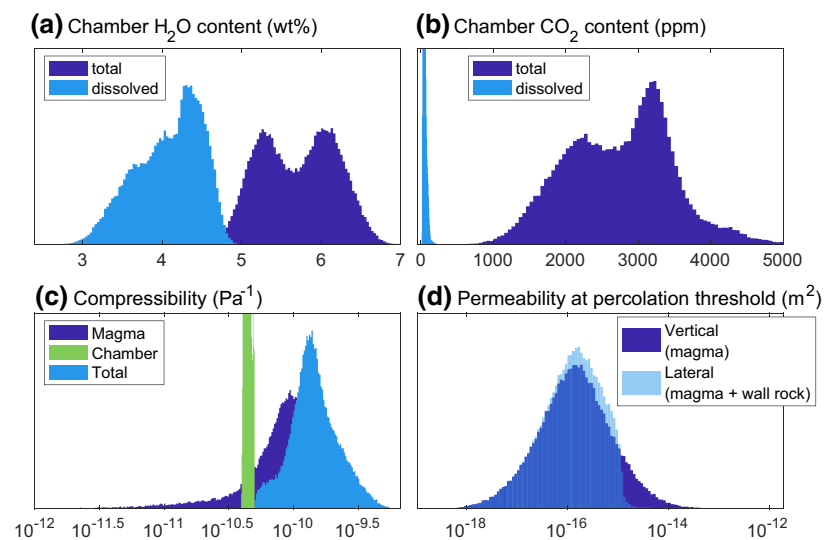
Figure 9. Posterior probability density functions of (a) total and dissolved H_2O content in the chamber, (b) total and dissolved CO_2 content in the chamber (note low dissolved content), (c) magma compressibility in the chamber and the chamber compressibility, and (d) vertical and lateral permeability at the percolation threshold depth.
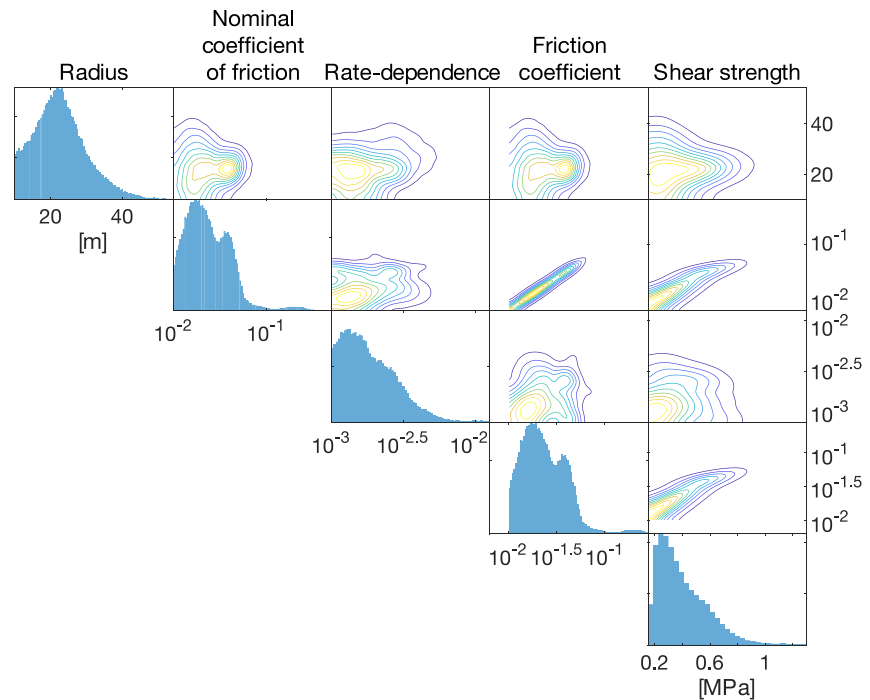
Figure 10. Correlation plots of frictional parameters. Conduit radius, nominal coefficient, and rate-dependence are directly estimated, while the friction coefficient at the reference velocity $v_r = 10^{-5}$ m/s and shear strength are dependent variables.

conduit. This corresponds to a magma compressibility of 0.2–2.7×10^{-10} Pa^{-1}. Chamber compressibility, which depends on the shape of the chamber and elastic modulus of the crust (here 20 GPa), has a very narrow range, thus magma compressibility largely controls the total compressibility which ranges from 0.7–3.1×10^{-10} Pa^{-1}.

The exsolved phase may be lost through permeable gas escape, both vertically through the conduit column and laterally through the conduit walls. The magma permeability scale is well constrained at 1.8×10^{-15}–7.2×10^{-13} m^2, and the percolation threshold is 0.21–0.28. Vertical gas escape only depends on the magma permeability, which ranges between 8.2×10^{-18}–2.4×10^{-15} m^2. Lateral gas escape depends on the magma and wall-rock permeability. However, at the percolation threshold, wall-rock permeability spans a narrow range of 1.1–2.2×10^{-15} m^2 (Manning & Ingebritsen, 1999) and is generally higher than magma permeability. Magma permeability is thus the limiting factor for lateral gas escape. This causes the distribution for both permeabilities to be approximately equal.

3.2.3. Conduit Friction

Extruded volume is the main control on conduit friction due to its relationship with extrusion rate (Figure 7). In contrast, ensemble appraisal using only the deformation data set produces broader distributions on both frictional parameters. When combining extruded volume and deformation data, posterior probabilities of friction become narrower. Since predicted gas emissions depend on the pressure gradient in the plug which is affected by frictional resistance, the ensemble appraisal with all data sets results in a well-constrained nominal frictional coefficient. The marginal posterior PDFs suggest that the nominal friction coefficient is low ($10^{-1.9}$–$10^{-1.3}$), while the rate-dependence of friction ranges between $10^{-3.0}$–$10^{-2.4}$. We will discuss these low values in Section 4. This corresponds to friction coefficients between 0.014 and 0.057 at the reference velocity $v = v_r = 10^{-5}$ m/s (Figure 10). Shear strength is given by $f\sigma_c$ where σ_c is the effective normal stress. At the plug depth (0.76–0.96 km), shear strength ranges between 0.23 and 0.82 MPa.

4. Discussion

Traditional geodetic inversions have used continuous and campaign GPS data from the Mount St. Helens 2004–2008 eruption to constrain the geometry and volume change of the chamber (Lisowski et al., 2008; Palano et al., 2012). Using a source model of three colocated orthogonal dislocations, Lisowski et al. (2008) obtain a chamber with an aspect ratio of 0.66 centered at 7.99 km depth with a volume change of 11.9 million m^3 in the first year of eruption. Applying the Yang et al. (1988) model for ellipsoidal chambers, Palano et al. (2012) found a more elongated chamber with aspect ratio 0.10 at a similar depth with a volume change of 7.97 million m^3 in the first 2 years of the eruption. Notably, the discrepancy in aspect ratio between the two studies arises from the difference in source model, because the predicted spatial pattern of deformation is approximately the same in both studies.

In this study, we applied the source model from Yang et al. (1988) as it satisfies the free surface boundary condition and, in the limit where the chamber is deep relative to the chamber dimensions, the pressure boundary condition on the chamber walls. Therefore our results align more closely with Palano et al. (2012) to prefer a more elongate chamber. The highest likelihood chamber has an aspect ratio of 0.30 with a volume change of 36 million m^3 over the whole eruption. The chamber centroid is located at 11 km depth. The volume change estimated in this inversion is about 3–4 times larger than Lisowski et al. (2008) and Palano et al. (2012) respectively due to both the longer time interval considered and also the deeper centroid location (Figure 8a). The top of the chamber, located at 4.6 km, has a pressure of 121 MPa. This is close to petrologic constraints, which find that plagioclase phenocrysts continued to grow until pressure decreased to 130 MPa (corresponding to 5 km depth) when magma exits the chamber and enters the conduit (Pallister et al., 2008; Rutherford & Devine, 2008).

Incorporating a physics-based model and extruded volume data enables us to resolve pressure change and chamber volume, which traditional geodetic inversions are unable to do. Although Palano et al. (2012) obtained a plausible volume change, their preferred model has a pressure change of 1,000 MPa and a chamber of volume of only 0.306 km^3. This large pressure change is inconsistent with the tensile strength of rock which is on the order of 10 MPa. Using a physics-based model with extrusion flux and deformation data, Anderson and Segall (2013) modeled a pressure decrease of 2–10 MPa over the course of the eruption. Combined with the volume change of 16–40 million m^3 constrained by deformation, they estimate the chamber to be at least 40 km^3 and reaching the upper bound of the inversion at 200 km^3. In this study, the 90% credible interval of the resampled models have pressure change 2–18 MPa and volume loss 20–66 million m^3, implying a chamber volume of 64–256 km^3. This represents a volume of material that deforms like a fluid on the time scale of the eruption and may contain regions of relatively high solid fraction. Total extruded volume scales as $\left(\beta_{mag} + \beta_{ch} \right) \Delta p_{ch} V_0$ (Segall, 2013). Given the final extruded volume of 94.2 million m^3 and typical system compressibility of $0.7 - 3.1 \times 10^{-10}$ Pa^{-1}, this implies a chamber volume on the order of 10^2 km^3, consistent with our posterior PDFs. A similar analysis in Mastin et al. (2009) obtained a smaller chamber volume estimate of 10–25 km^3 using a similar pressure change but 4–5 times higher magma compressibility. This difference in compressibility arises because Mastin et al. (2009) used a fixed crystal volume fraction in the chamber, while we include the increase in density due to crystallization, which counteracts some of the decrease in density caused by gas exsolution and expansion. As a result, compressibilities obtained in this study are lower. Changes to the crystallization model, such as by relaxing the isothermal assumption, could increase magma compressibility and bring the chamber volume closer to values suggested in Mastin et al. (2009). Release of latent heat during crystallization has been shown to increase magma temperature by up to 75°C (Blundy et al., 2006). An adiabatic model would delay crystallization and allow higher magma compressibility. In the conduit, plug formation may be delayed by a few 100 m. Including energy conservation in the model would thus improve constraints on the chamber volume and plug depth.

Independent estimates of chamber volume at Mount St. Helens span a wide range from a few km^3 to ~1,000 km^3. Eruption volumes can offer a lower bound on chamber size. The largest plinian eruption in the Holocene produced 2.3 km^3 of material (Nathenson, 2017). However, given that Mount St. Helens has more frequently produced lava flows and domes, the more common eruption volumes are smaller (Clynne et al., 2008; Pallister et al., 2017). Earthquake hypocenters in the 1980s show distinct lobes surrounding an earthquake-free zone, thought to be the semiliquid magma body, of about 10–20 km^3 (Scan-

done & Malone, 1985). Recent seismic tomography in the iMUSH experiment found a body with low shear wave velocities at 4–13 km depth and spanning 15 km wide, corresponding to a volume ~1,000 km³ (Kiser et al., 2016). Our inversions agree with the vertical extent of the chamber but suggest a more limited horizontal extent. The volume from tomography is an upper bound due to resolution limitations, and the melt fraction causing the reduction in shear wave velocities is uncertain. Petrologic observations of compositionally diverse magma batches with different stagnation depths suggest that the volume estimated by the iMUSH experiment may reflect a mush containing distinct regions of high melt fraction (Leeman & Smith, 2018; Wanke, Clynne, et al., 2019; Wanke, Karakas, et al., 2019). This would be consistent with geologic evidence of smaller eruption volumes. Reconciling the discrepancy between our inversion results and the geologic perspective would require more realistic geodetic source models for a mush system containing distinct high melt fraction bodies.

Gas solubility modeling using VolatileCalc (Newman & Lowenstern, 2002) constrained by carbon dioxide emissions and extruded volume give 4.4 wt% dissolved H_2O and 37 ppm dissolved CO_2 at 130 MPa, the pressure at the top of the magma chamber assumed at 5 km depth (Gerlach et al., 2008). This is consistent with our inversion estimates of 3.3–4.6 wt% dissolved H_2O and 22–100 ppm dissolved CO_2. The same gas solubility modeling suggests a porosity 10.11%–10.85% at 130 MPa (Gerlach et al., 2008). At similar pressures, our inversion results give a porosity of 5.5%–10.5%. There are some models with higher porosities at the conduit base (up to 20%), but these have shorter conduit lengths, so their conduit base pressure is lower, allowing gas to exsolve and expand. The May 18, 1980 magma at Mount St. Helens had a porosity of over 15% (equivalent to 3% by weight) at its equilibration pressure of 220 MPa (Gerlach et al., 2008; Rutherford, 1993; Wallace, 2001). Assuming 0.67 mole fraction of water in the exsolved phase (Rutherford, 1993), this corresponds to ~37% porosity at 130 MPa. Thus at comparable pressures, the 2004–2008 magma has a much lower exsolved volume than the May 18, 1980 magma, consistent with the interpretation that the the 2004–2008 magma was depleted in volatiles relative to the May 18, 1980 magma.

Melt inclusions in amphiboles and plagioclase suggest dissolved H_2O contents up to 3.6 wt%, however most are below 3 wt% which is considered low for the magma equilibration pressure of 130 MPa (Blundy et al., 2008; Pallister et al., 2008). This suggests that melt inclusions may have ruptured or crystallized during ascent and might not be representative of the actual dissolved water content in the chamber (Blundy et al., 2008; Pallister et al., 2008; Rutherford & Devine, 2008). Our inversions, which give dissolved water contents above 3 wt%, support this interpretation.

The magma permeability scale k_c controls the balance between chamber volatile contents and observed dome porosity, because the distribution of k_c remains consistent across all four appraisals. This control is consistent with inversions using the steady-state version of this conduit flow model (Wong et al., 2017). However, Wong et al. (2017) found a tight constraint on $k_c \sim 10^{-12.3} - 10^{-10.5}$ m², while the distribution derived here finds lower k_c. We attribute this difference to the steady-state assumption as discussed in Section 4.3 of Wong and Segall (2019). Since each steady-state solution is independent, the solution adjusts to ensure that magma and gas flux into the region above the percolation threshold is sufficient to sustain gas escape. The magma column remains gas-rich even with extensive gas escape due to high permeability allowing extensive gas ascent. In time-dependent solutions, however, high magma permeability allows a large proportion of volatiles to be lost to the surroundings at early time, substantially decreasing the amount of gas in the shallow conduit. This causes the eruption velocity to slow down drastically which is inconsistent with the extruded volume time series. Therefore, this high permeability constant is no longer preferred. Instead, an intermediate value that allows only moderate gas escape is preferred.

Laboratory measurements of permeability in the Mount St. Helens plug found vertical permeability of 10^{-14} m² in the margins and 10^{-15} m² in the core of the lava dome (Gaunt et al., 2014). Horizontal permeability was found to be 10^{-18} m² in the margins and 10^{-15} m² in the core (Gaunt et al., 2014). Our modeled permeability captures this range of values with few models having permeability greater than 10^{-14} m², although it does not account for the anisotropy observed in the experiments. Two-dimensional numerical models suggest that at shallow depths, gases tend to concentrate near the conduit margins which enhances

gas escape (Collombet, 2009). This is corroborated by ring-shaped degassing observations at Santiaguito volcano in Guatemala (Bluth & Rose, 2004).

Furtwhermore, we do not consider the impact of crystals on gas percolation. Experiments have shown that the presence of crystals can enhance bubble nucleation and can control bubble size (Belien et al., 2010; Spina et al., 2016). Channelization of gas flow may occur at high crystal contents particularly in magmas with elongated crystals, leading to efficient gas migration (Oppenheimer et al., 2015; Spina et al., 2016). Three-dimensional, pore-scale simulations better capture this spatially localized mode of degassing (De-gruyter et al., 2019; Parmigiani et al., 2016). In contrast, this study focuses on the macroscale impact of gas escape on extrusion flux, ground deformation, and gas emissions, which are unable to resolve the spatial heterogeneity of gas flow.

Inversion results suggest a narrow conduit of radius 12–36 m. Previous inversions with the steady-state conduit model used extrusion velocity observed by remote cameras (Major et al., 2008) and extrusion flux to estimate the conduit radius, giving a best fit radius of 148 m (Wong et al., 2017). Deformation was not included as a constraint in Wong et al. (2017). In this inversion, we omitted the extrusion velocity as a constraint because it may only reflect the near-surface conduit geometry. Flaring conduit geometries have been seen in the rare cases where we have camera observations a few 100 m into conduits (Johnson et al., 2018; Lyons et al., 2016; Moussallam et al., 2016). Mechanical modeling also shows that conduit collapse during explosive eruptions can create the flared geometry at the top (Aravena et al., 2017; Macedonio et al., 1994; Mitchell, 2005). Therefore including the extrusion velocity may bias results toward conduit radii larger than the average radius of the conduit.

Information from the total extrusion volume and deformation at the end of the eruption, as well as their rate of change, provide constraints on radius, as seen in sensitivity analyses of Wong and Segall (2019). In Poiseuille Flow with constant material properties, doubling the conduit radius increases the velocity and mass flow rate by four and eight times respectively. In this model, the extent of velocity increase may be affected by gas escape and frictional properties. Increasing velocity will increase the rate of pressure decay because it is proportional to mass flow rate (Equation 10). To maintain the same mass flow rate, one would need to reduce the chamber overpressure, but this would degrade the fit to the total extruded volume and radial displacements. One could also increase chamber volume, however this would alter the relative magnitudes of extruded volume and radial displacements. The conduit radii of 12–36 m balance these competing effects to ensure fit to the data.

The smaller radius may also explain the higher pressure over magmastatic and the lower friction coefficient estimated here compared to the distribution obtained from the steady-state model. Previous inversions using the steady-state conduit model already estimated low $f_0(10^{-2} - 10^{-0.25})$, with the maximum *a posteriori* model having $f_0 = 0.46$ (Wong et al., 2017). The conduit model only resolves shear strength on the conduit walls $f(\sigma - p_{hyd})$, where the normal stress σ was assumed to be lithostatic and the pore pressure p_{hyd} was assumed to be hydrostatic. Decreasing σ by considering topographic or tectonic effects could result in higher f_0. Elevated pore pressures due to gases escaping laterally and localizing on the conduit margins may also increase the estimated f_0. Even so, the f_0 estimated in this study are lower than in Wong et al. (2017), suggesting that other reasons, such as the narrower conduit, must cause the low friction estimated with the time-dependent model. A narrower conduit has a higher ratio of surface area to cross-sectional area. To maintain the same flow rate requires an increase in the driving force for flow, or a reduction in the viscous and/or frictional losses. The slight positive correlation between radius and the nominal friction coefficient (Figure 10) suggests that within the limited range of radii that fit the data, the friction coefficient is lower for narrower conduits. Of course, inaccuracies in the model for magma viscosity will trade off with estimates of the frictional resistance. Viscosity models that predict lower viscosity for a given crystal fraction compared to the Costa (2005) model would reduce viscous losses, therefore requiring greater frictional losses through a higher friction coefficient to achieve the same mass flow rate.

5. Conclusion

In this study, we applied a simple physics-based model to estimate properties of the magmatic system at Mount St. Helens based on diverse time series data from the 2004–2008 eruption. The model is specialized for dome-forming eruptions, taking into account pressure-dependent crystallization, volatile exsolution, and gas escape during magma ascent. These processes cause magma that is flowing viscously at depth to transition to solid plug sliding at shallow depth, ultimately extruding a dome in the crater. To constrain important parameters in the model, we jointly apply extruded volume, continuous and campaign GPS positions, and carbon dioxide emissions time series from the eruption in an inversion using the neighborhood algorithm (Sambridge, 1999b, 1999a).

Key findings of the inversion include:

1. We are able to find models that fit the extruded volume, ground deformation, and carbon dioxide emissions from the 2004–2008 eruption at Mount St. Helens. In particular, the best fit model approximately captures the rapid decay in JRO1 radial displacement while maintaining satisfactory fits to the other data sets, which previous studies were unable to replicate.
2. The data prefer elongate chambers with aspect ratios 0.13–0.55, located at 9–17 km depth with chamber volumes of 64–256 km^3. These chamber volumes suggest that solutions to the full time-dependent governing equations is needed to model the temporal evolution of the eruption. Volume lost from the chamber is 20–66 million m^3.
3. The top of the chamber has total (dissolved and exsolved) water contents of 5.0–6.4 wt% and carbon dioxide contents of 1,600–3,900 ppm. At 130 MPa, which is the top of the magma chamber inferred from plagioclase phase equilibrium, this corresponds to a porosity of 5.5%–10.5%.
4. Excess exsolved volatiles escape the system vertically through the conduit and laterally through the conduit walls. The magma permeability scale is well-constrained by the porosity of the dome rock.
5. Compared to previous inversions using the steady-state conduit model (Wong et al., 2017), this inversion using the time-dependent model suggests a lower magma permeability scale because of differences in the mechanism for gas escape in steady-state and time-dependent conduit flow models. In addition, a narrower conduit of radius 12–36 m is preferred. This may account for the higher pressure over magmastatic (13–55 MPa) and lower conduit wall friction coefficients (0.014–0.057 at the reference velocity $v = v_r = 10^{-5}$ m/s). A weaker dependence of viscosity on crystal fraction would allow larger friction coefficients.

Data Availability Statement

Code used and developed in this study are available here: conduit model (http://doi.org/10.5281/zenodo.3969094), parameter estimation (http://doi.org/10.5281/zenodo.3969103), inversions for Mount St. Helens (http://doi.org/10.5281/zenodo.3969090), inversion results files (http://doi.org/10.5281/zenodo.3969105). Data from the Mount St. Helens eruption are available from Schilling et al. (2008), Lisowski et al. (2008), Gerlach et al. (2008), and Dzurisin et al. (2015), as well as the USGS Pacific Northwest GPS Network (https://earthquake.usgs.gov/monitoring/gps/Pacific_Northwest).

References

Albino, F., Pinel, V., Massol, H., & Collombet, M. (2011). Conditions for detection of ground deformation induced by conduit flow and evolution. *Journal of Geophysical Research*, *116*(6), B06201. https://doi.org/10.1029/2010JB007871

Amoruso, A., & Crescentini, L. (2009). Shape and volume change of pressurized ellipsoidal cavities from deformation and seismic data. *Journal of Geophysical Research*, *114*(B2), B02210. https://doi.org/10.1029/2008JB005946

Anderson, K., Lisowski, M., Segall, P. (2010). Cyclic ground tilt associated with the 2004–2008 eruption of Mount St. Helens. *Journal of Geophysical Research*, *115*(B11), B11201. https://doi.org/10.1029/2009jb007102

Anderson, K., & Segall, P. (2011). Physics-based models of ground deformation and extrusion rate at effusively erupting volcanoes. *Journal of Geophysical Research*, *116*(B7), B07204. http://dx.doi.org/10.1029/2010jb007939

Anderson, K., & Segall, P. (2013). Bayesian inversion of data from effusive volcanic eruptions using physics-based models: Application to Mount St. Helens 2004–2008. *Journal of Geophysical Research: Solid Earth*, *118*(5), 2017–2037. https://doi.org/10.1002/jgrb.50169

Aravena, Á., de' Michieli Vitturi, M., Cioni, R., Neri, A. (2017). Stability of volcanic conduits during explosive eruptions. *Journal of Volcanology and Geothermal Research*, *339*, 52–62. https://dx.doi.org/10.1016/j.jvolgeores.2017.05.003

Belien, I. B., Cashman, K. V., & Rempel, A. W. (2010). Gas accumulation in particle-rich suspensions and implications for bubble populations in crystal-rich magma. *Earth and Planetary Science Letters*, *297*(1–2), 133–140. https://doi.org/10.1016/j.epsl.2010.06.014

Blower, J. (2001). Factors controlling permeability-porosity relationships in magma. *Bulletin of Volcanology*, *63*, 497–504. https://doi.org/10.1007/s004450100172

Blundy, J., Cashman, K. V., & Berlo, K. (2008). Evolving magma storage conditions beneath Mount St. Helens inferred from chemical variations in melt inclusions from the 1980-1986 and current (2004-2006) eruptions. *A volcano rekindled: The renewed eruption of Mount St. Helens 2004-2006*. U.S. Geological Survey Professional Paper 1750, pp. 755–790. Washington, DC: U.S. Government Printing Office.

Blundy, J., Cashman, K., & Humphreys, M. (2006). Magma heating by decompression-driven crystallization beneath andesite volcanoes. *Nature*, *443*(7107), 76–80. https://doi.org/10.1038/nature05100

Bluth, G. J., & Rose, W. I. (2004). Observations of eruptive activity at Santiaguito volcano, Guatemala. *Journal of Volcanology and Geothermal Research*, *136*(3–4), 297–302. https://doi.org/10.1016/j.jvolgeores.2004.06.001

Caricchi, L., Burlini, L., Ulmer, P., Gerya, T., Vassalli, M., & Papale, P. (2007). Non-Newtonian rheology of crystal-bearing magmas and implications for magma ascent dynamics. *Earth and Planetary Science Letters*, *264*(3–4), 402–419. https://doi.org/10.1016/j.epsl.2007.09.032

Cashman, K. V., Thornber, C., & Pallister, J. S. (2008). From dome to dust: Shallow crystallization and fragmentation of conduit magma during the 2004–2006 dome extrusion of Mount St. Helens, Washington. In *A volcano rekindled: The renewed eruption of Mount St. Helens 2004–2006*. U.S. Geological Survey Professional Paper 1750, pp. 387–413. Washington, DC: U.S. Government Printing Office.

Clarke, A. B., Stephens, S., Teasdale, R., Sparks, R. S. J., & Diller, K. (2007). Petrologic constraints on the decompression history of magma prior to Vulcanian explosions at the Soufriere Hills volcano, Montserrat. *Journal of Volcanology and Geothermal Research*, *161*(4), 261–274. https://doi.org/10.1016/j.jvolgeores.2006.11.007

Clynne, M. A., Calvert, A. T., Wolfe, E. W., Evarts, R. C., Fleck, R. J., & Lanphere, M. A. (2008). *The pleistocene eruptive history of Mount St. Helens, Washington, from 300,000 to 12,800 years before present*. U.S. Geological Survey Professional Paper 1750, pp. 593–628. Washington, DC: U.S. Government Printing Office. https://doi.org/10.3133/pp17502

Collombet, M. (2009). Two-dimensional gas loss for silicic magma flows: Toward more realistic numerical models. *Geophysical Journal International*, *177*(1), 309–318. https://doi.org/10.1111/j.1365-246X.2008.04086.x

Costa, A. (2005). Viscosity of high crystal content melts: Dependence on solid fraction. *Geophysical Research Letters*, *32*(22), L22308. https://doi.org/10.1029/2005GL024303

Crowell, B. W., Bock, Y., & Liu, Z. (2016). Single-station automated detection of transient deformation in GPS time series with the relative strength index: A case study of Cascadian slow slip. *Journal of Geophysical Research: Solid Earth*, *121*(12), 9077–9094. https://doi.org/10.1002/2016JB013542

Degruyter, W., Parmigiani, A., Huber, C., & Bachmann, O. (2019). How do volatiles escape their shallow magmatic hearth? *Philosophical Transactions of the Royal Society A: Mathematical, Physical and Engineering Sciences*, *377*(2139), 20180017. Retrieved from http://www.royalsocietypublishing.org/doi/10.1098/rsta.2018.0017

Denlinger, R. P., & Hoblitt, R. P. (1999). Cyclic eruptive behavior of silicic volcanoes. *Geology*, *27*(5), 459–462. https://doi.org/10.1130/0091-7613(1999)027%3C0459:CEBOSV%3E2.3.CO;2

De' Micheli Vitturi, M., Clarke, A. B., Neri, A., & Voight, B. (2013). Extrusion cycles during dome-building eruptions. *Earth and Planetary Science Letters*, *371–372*, 37–48. https://doi.org/10.1016/j.epsl.2013.03.037

Diller, K., Clarke, A. B., Voight, B., & Neri, A. (2006). Mechanisms of conduit plug formation: Implications for vulcanian explosions. *Geophysical Research Letters*, *33*(20), L20302. https://doi.org/10.1029/2006GL027391

Dzurisin, D., Moran, S. C., Lisowski, M., Schilling, S. P., Anderson, K. R., & Werner, C. (2015). The 2004-2008 dome-building eruption at Mount St. Helens, Washington: Epilogue. *Bulletin of Volcanology*, *77*(10), 89. https://doi.org/10.1007/s00445-015-0973-4

Fukushima, Y., Cayol, V., & Durand, P. (2005). Finding realistic dike models from interferometric synthetic aperture radar data: The February 2000 eruption at Piton de la Fournaise. *Journal of Geophysical Research*, *110*(B3), B03206. https://doi.org/10.1029/2004JB003268

Gaunt, H. E., Sammonds, P. R., Meredith, P. G., Smith, R., & Pallister, J. S. (2014). Pathways for degassing during the lava dome eruption of Mount St. Helens 2004-2008. *Geology*, *42*(11), 947–950. https://doi.org/10.1130/G35940.1

Gerlach, T. M., Mcgee, K. A., & Doukas, M. P. (2008). Emission rates of CO_2, SO_2, and H_2S, scrubbing, and preeruption excess volatiles at Mount St. Helens, 2004-2005. *A volcano rekindled: The renewed eruption of Mount St. Helens 2004–2006*. U.S. Geological Survey Professional Paper 1750, pp. 543–571. Washington, DC: U.S. Government Printing Office.

Ghiorso, M. S., & Sack, R. O. (1995). Chemical mass transfer in magmatic processes IV. A revised and internally consistent thermodynamic model for the interpolation and extrapolation of liquid-solid equilibria in magmatic systems at elevated temperatures and pressures. *Contributions to Mineralogy and Petrology*, *119*(2–3), 197–212. https://doi.org/10.1007/BF00307281

Gonnermann, H. M., & Manga, M. (2007). The fluid mechanics inside a volcano. *Annual Review of Fluid Mechanics*, *39*, 321–356. https://doi.org/10.1146/annurev.fluid.39.050905.110207

Iverson, R. M. (2008). Dynamics of seismogenic volcanic extrusion resisted by a solid surface plug, Mount St. Helens, 2004–2005. In *A volcano rekindled: The renewed eruption of Mount St. Helens 2004–2006. U.S. Geological Survey Professional Paper 1750*, 425–460). Washington, DC: U.S. Government Printing Office.

Jaupart, C., & Allègre, C. J. (1991). Gas content, eruption rate and instabilities of eruption regime in silicic volcanoes. *Earth and Planetary Science Letters*, *102*(3–4), 413–429. https://doi.org/10.1016/0012-821X(91)90032-D

Johnson, J. B., Watson, L. M., Palma, J. L., Dunham, E. M., & Anderson, J. F. (2018). Forecasting the eruption of an open-vent volcano using resonant infrasound tones. *Geophysical Research Letters*, *45*(5), 2213–2220. https://doi.org/10.1002/2017GL076506

Kawaguchi, R., & Nishimura, T. (2015). Numerical investigation of temporal changes in volcanic deformation caused by a gas slug ascent in the conduit. *Journal of Volcanology and Geothermal Research*, *302*, 1–10. https://doi.org/10.1016/j.jvolgeores.2015.06.002

Kiser, E., Palomeras, I., Levander, A., Zelt, C., Harder, S., Schmandt, B., et al. (2016). Magma reservoirs from the upper crust to the Moho inferred from high-resolution Vp and Vs models beneath Mount St. Helens, Washington State, USA. *Geology*, *44*(6), G37591.1. https://doi.org/10.1130/G37591.1

Klug, C., & Cashman, K. V. (1996). Permeability development in vesiculating magmas: Implications for fragmentation. *Bulletin of Volcanology*, *58*, 87–100. https://doi.org/10.1007/s004450050128

Kozono, T., & Koyaguchi, T. (2012). Effects of gas escape and crystallization on the complexity of conduit flow dynamics during lava dome eruptions. *Journal of Geophysical Research*, *117*(B8), B08204. https://doi.org/10.1029/2012JB009343

Langbein, J. (2004). Noise in two-color electronic distance meter measurements revisited. *Journal of Geophysical Research*, *109*(B4), B04406. https://doi.org/10.1029/2003JB002819

Leeman, W. P., & Smith, D. R. (2018). The role of magma mixing, identification of mafic magma inputs, and structure of the underlying magmatic system at Mount St. Helens. *American Mineralogist*, *103*(12), 1925–1944. https://doi.org/10.2138/am-2018-6555

Leonard, B. P. (1995). Order of accuracy of QUICK and related convection-diffusion schemes. *Applied Mathematical Modelling*, *19*(11), 640–653. https://doi.org/10.1016/0307-904X(95)00084-W

Lisowski, M., Dzurisin, D., Denlinger, R. P., & Iwatsubo, E. Y. (2008). Analysis of GPS-measured deformation associated with the 2004–2006 dome-building eruption of Mount St. Helens, Washington. In *A volcano rekindled: The renewed eruption of Mount St. Helens 2004–2006. U.S. Geological Survey Professional Paper 1750,* pp. 301–333. Washington, DC: U.S. Government Printing Office.

Liu, Y., Zhang, Y., & Behrens, H. (2005). Solubility of H_2O in rhyolitic melts at low pressures and a new empirical model for mixed H_2O-CO_2 solubility in rhyolitic melts. *Journal of Volcanology and Geothermal Research*, *143*(1–3), 219–235. https://doi.org/10.1016/j.jvolgeores.2004.09.019

Llewellin, E. W., & Manga, M. (2005). Bubble suspension rheology and implications for conduit flow. *Journal of Volcanology and Geothermal Research*, *143*(1–3), 205–217. https://doi.org/10.1016/j.jvolgeores.2004.09.018

Lyons, J. J., Haney, M. M., Werner, C., Kelly, P., Patrick, M., Kern, C., & Trusdell, F. (2016). Long period seismicity and very long period infrasound driven by shallow magmatic degassing at Mount Pagan, Mariana Islands. *Journal of Geophysical Research: Solid Earth*, *121*(1), 188–209. https://doi.org/10.1002/2015JB012490

Macedonio, G., Dobran, F., & Neri, A. (1994). Erosion processes in volcanic conduits and application to the AD 79 eruption of Vesuvius. *Earth and Planetary Science Letters*, *121*, 137–152. https://doi.org/10.1016/0012-821X(94)90037-X

Major, J. J., Kingsbury, C. G., Poland, M. P., & Lahusen, R. G. (2008). Extrusion rate of the Mount St. Helens lava dome estimated from terrestrial imagery, November 2004–December 2005. *A volcano rekindled: The renewed eruption of Mount St. Helens 2004–2006*. U.S. Geological Survey Professional Paper 1750, pp. 237–255. Washington, DC: U.S. Government Printing Office.

Manning, C. E., & Ingebritsen, S. E. (1999). Permeability of the continental crust: Implications of geothermal data and metamorphic systems. *Reviews of Geophysics*, *37*(1), 127–150.

Mao, A., Harrison, C. G. A., & Dixon, T. H. (1999). Noise in GPS coordinate time series. *Journal of Geophysical Research*, *104*(B2), 2797–2816. https://doi.org/10.1029/1998JB900033

Mastin L. G. (2002). Insights into volcanic conduit flow from an open-source numerical model. *Geochemistry, Geophysics, Geosystems*, *3*(7), 1–18. http://dx.doi.org/10.1029/2001gc000192

Mastin, L. G., Lisowski, M., Roeloffs, E., & Beeler, N. (2009). Improved constraints on the estimated size and volatile content of the Mount St. Helens magma system from the 2004-2008 history of dome growth and deformation. *Geophysical Research Letters*, *36*(20), L20304. https://doi.org/10.1029/2009GL039863

Melnik, O., & Sparks, R. S. J. (2005). Controls on conduit magma flow dynamics during lava dome building eruptions. *Journal of Geophysical Research*, *110*(B2), B02209. https://doi.org/10.1029/2004JB003183

Mitchell, K. L. (2005). Coupled conduit flow and shape in explosive volcanic eruptions. *Journal of Volcanology and Geothermal Research*, *143*(1–3), 187–203. https://doi.org/10.1016/j.jvolgeores.2004.09.017

Moran, S. C., Malone, S. D., Qamar, A. I., Thelen, W. A., Wright, A. K., & Caplan-Auerbach, J. (2008). Seismicity associated with renewed dome building at Mount St. Helens, 2004-2005. In *A volcano rekindled: The renewed eruption of Mount St. Helens 2004-2006*. U.S. Geological Survey Professional Paper 1750, 27–60. Washington, DC: U.S. Government Printing Office.

Moussallam, Y., Bani, P., Curtis, A., Barnie, T., Moussallam, M., Peters, N., et al. (2016). Sustaining persistent lava lakes: Observations from high-resolution gas measurements at Villarrica volcano, Chile. *Earth and Planetary Science Letters*, *454*, 237–247. https://doi.org/10.1016/j.epsl.2016.09.012

Nathenson, M. (2017). Revised tephra volumes for Cascade Range volcanoes. *Journal of Volcanology and Geothermal Research*, *341*, 42–52. https://doi.org/10.1016/j.jvolgeores.2017.04.021

Neuberg, J. W., Collinson, A. S., Mothes, P. A., Ruiz, C. M., & Aguaiza, S. (2018). Understanding cyclic seismicity and ground deformation patterns at volcanoes: Intriguing lessons from Tungurahua volcano, Ecuador. *Earth and Planetary Science Letters*, *482*, 193–200. https://doi.org/10.1016/j.epsl.2017.10.050

Newman, S., & Lowenstern, J. B. (2002). Volatile Calc: A silicate melt–H_2O–CO_2 solution model written in Visual Basic for excel. *Computers & Geosciences*, *28*, 597–604. https://doi.org/10.1016/S0098-3004(01)00081-4

Oppenheimer, J., Rust, A. C., Cashman, K. V., & Sandnes, B. (2015). Gas migration regimes and outgassing in particle-rich suspensions. *Frontiers in Physics*, *3*, 1–13. https://doi.org/10.3389/fphy.2015.00060

Palano, M., Guarrera, E., & Mattia, M. (2012). GPS ground deformation patterns at Mount St. Helens (Washington, USA) from 2004 to 2010. *Terra Nova*, *24*(2), 148–155. https://doi.org/10.1111/j.1365-3121.2011.01049.x

Pallister, J. S., Clynne, M. A., Wright, H. M., Eaton, A. R. V., Vallance, J. W., Sherrod, D. R., & Kokelaar, B. P. (2017). *Field-trip guide to Mount St. Helens, Washington—An overview of the eruptive history and petrology, tephra deposits, 1980 pyroclastic density current deposits, and the crater*. Scientific Investigations Report 2017-5022-D, pp. 1–65. https://doi.org/10.3133/sir20175022d

Pallister, J. S., Thornber, C. R., Cashman, K. V., Clynne, M. A., Lowers, H. A., Mandeville, C. W., et al. (2008). Petrology of the 2004–2006 Mount St. Helens lava dome—Implications for magmatic plumbing and eruption triggering. In *A volcano rekindled: The renewed eruption of Mount St. Helens 2004–2006. U.S. Geological Survey Professional Paper 1750*, 647–702). Washington, DC: U.S. Government Printing Office.

Papale, P. (2001). Dynamics of magma flow in volcanic conduits with variable fragmentation efficiency and nonequilibrium pumice degassing. *Journal of Geophysical Research*, *106*(B6), 11043–11065. https://doi.org/10.1029/2000JB900428

Parmigiani, A., Faroughi, S., Huber, C., Bachmann, O., & Su, Y. (2016). Bubble accumulation and its role in the evolution of magma reservoirs in the upper crust. *Nature*, *532*(7600), 492–495. https://doi.org/10.1038/nature17401

Plank, T., Kelley, K. a., Zimmer, M. M., Hauri, E. H., & Wallace, P. J. (2013). Why do mafic arc magmas contain ~4wt% water on average? *Earth and Planetary Science Letters*, *364*, 168–179. https://doi.org/10.1016/j.epsl.2012.11.044

Pritchard, M. E., & Simons, M. (2002). A satellite geodetic survey of large-scale deformation of volcanic centres in the central Andes. *Nature*, *418*(6894), 167–171. https://doi.org/10.1038/nature00872

Rice, J. R., Lapusta, N., & Ranjith, K. (2001). Rate and state dependent friction and the stability of sliding between elastically deformable solids. *Journal of the Mechanics and Physics of Solids*, *49*(9), 1865–1898. https://doi.org/10.1016/S0022-5096(01)00042-4

Rutherford, M. J. (1993). Experimental petrology applied to volcanic processes. *Eos, Transactions American Geophysical Union*, *74*(5), 49–55. https://doi.org/10.1029/93EO00142

Rutherford, M. J., & Devine, J. D. (2008). Magmatic conditions and processes in the storage zone of the 2004–2006 Mount St. Helens dacite. *A volcano rekindled: The renewed eruption of Mount St. Helens 2004-2006*. U.S. Geological Survey Professional Paper 1750, pp. 703–725. Washington, DC: U.S. Government Printing Office.

Saar, M. O., & Manga, M. (1999). Permeability-porosity relationship in vesicular basalts. *Geophysical Research Letters*, *26*(1), 111–114. https://doi.org/10.1029/1998GL900256

Sambridge, M. (1999b). Geophysical inversion with a neighbourhood algorithm-I. Searching a parameter space. *Geophysical Journal International*, *138*, 479–494.

Sambridge, M. (1999). Geophysical inversion with a neighborhood algorithm-II. Appraising the ensemble. *Geophysical Journal International*, *138*, 727–746.

Scandone, R., & Malone, S. D. (1985). Magma supply, magma discharge and readjustment of the feeding system of Mount St. Helens during 1980. *Journal of Volcanology and Geothermal Research*, *23*(3–4), 239–262. https://doi.org/10.1016/0377-0273(85)90036-8

Schilling, S. P., Thompson, R., Messerich, J., & Iwatsubo, E. Y. (2008). Use of digital aerophotogrammetry to determine rates of lava dome growth, Mount St. Helens, Washington, 2004–2005. In *A volcano rekindled: The renewed eruption of Mount St. Helens 2004–2006*. U.S. Geological Survey Professional Paper 1750, pp. 145–167. Washington, DC: U.S. Government Printing Office.

Schneider, A., Rempel, A. W., & Cashman, K. V. (2012). Conduit degassing and thermal controls on eruption styles at Mount St. Helens. *Earth and Planetary Science Letters*, *357–358*, 347–354. https://doi.org/10.1016/j.epsl.2012.09.045

Scott, W. E., Sherrod, D. R., & Gardner, C. A. (2008). Overview of the 2004 to 2006, and continuing, eruption of Mount St. Helens, Washington. *A volcano rekindled: The renewed eruption of Mount St. Helens, 2004-2006*. US Geological Survey Professional Paper 1750, 3–22). Washington, DC: U.S. Government Printing Office.

Segall, P. (2013). Volcano deformation and eruption forecasting. *Geological Society, London, Special Publications*, *380*, 85–106. https://doi.org/10.1144/SP380.4

Smith, R., Sammonds, P. R., Tuffen, H., & Meredith, P. G. (2011). Evolution of the mechanics of the 2004-2008 Mt. St. Helens lava dome with time and temperature. *Earth and Planetary Science Letters*, *307*(1–2), 191–200. https://doi.org/10.1016/j.epsl.2011.04.044

Sparks, R. S. J. (2003). Forecasting volcanic eruptions. *Earth and Planetary Science Letters*, *210*, 1–15. https://doi.org/10.1016/S0012-821X(03)00124-9

Spina, L., Cimarelli, C., Scheu, B., Di Genova, D., & Dingwell, D. B. (2016). On the slow decompressive response of volatile- and crystal-bearing magmas: An analogue experimental investigation. *Earth and Planetary Science Letters*, *433*, 44–53. https://doi.org/10.1016/j.epsl.2015.10.029

Thornber, C. R., Pallister, J. S., Rowe, M. C., Mcconnell, S., Herriott, T. M., Eckberg, A., et al. (2008). *Catalog of Mount St. Helens 2004–2007 dome samples with major- and trace-element chemistry (Open-File Report 2008-1130 Technical Report)*. U.S. Geological Survey.

Vallance, J., Schneider, D., & Schilling, S. (2008). Growth of the 2004–2006 lava-dome complex at Mount St. Helens, Washington. In *A volcano rekindled: The renewed Eruption of Mount St. Helens 2004–2006*. U.S. Geological Survey Professional Paper 1750, pp. 169–208. Washington, DC: U.S. Government Printing Office.

Wallace, P. J. (2001). Volcanic SO2 emissions and the abundance and distribution of exsolved gas in magma bodies. *Journal of Volcanology and Geothermal Research*, *108*(1–4), 85–106. https://doi.org/10.1016/S0377-0273(00)00279-1

Wanke, M., Clynne, M. A., von Quadt, A., Vennemann, T. W., & Bachmann, O. (2019). Geochemical and petrological diversity of mafic magmas from Mount St. Helens. *Contributions to Mineralogy and Petrology*, *174*(1), 1–25. https://doi.org/10.1007/s00410-018-1544-4

Wanke, M., Karakas, O., & Bachmann, O. (2019). The genesis of arc dacites: The case of Mount St. Helens, WA. *Contributions to Mineralogy and Petrology*, *174*(1), 1–14. https://doi.org/10.1007/s00410-018-1542-6

Whittington, A. G., Hellwig, B. M., Behrens, H., Joachim, B., Stechern, A., & Vetere, F. (2009). The viscosity of hydrous dacitic liquids: Implications for the rheology of evolving silicic magmas. *Bulletin of Volcanology*, *71*(2), 185–199. https://doi.org/10.1007/s00445-008-0217-y

Williams, S. D. (2008). CATS: GPS coordinate time series analysis software. *GPS Solutions*, *12*(2), 147–153. https://doi.org/10.1007/s10291-007-0086-4

Wong, Y.-Q., & Segall, P. (2019). Numerical analysis of time-dependent conduit magma flow in dome-forming eruptions with application to Mount St. Helens 2004-2008. *Journal of Geophysical Research: Solid Earth*, *124*(11), 11251–11273. https://doi.org/10.1029/2019JB017585

Wong, Y.-Q., Segall, P., Bradley, A., & Anderson, K. (2017). Constraining the magmatic system at Mount St. Helens (2004-2008) using Bayesian inversion with physics-based models including gas escape and crystallization. *Journal of Geophysical Research: Solid Earth*, *122*(10), 7789–7812. https://doi.org/10.1002/2017JB014343

Yang, X.-M., Davis, P. M., & Dieterich, J. H. (1988). Deformation from inflation of a dipping finite prolate spheroid in an elastic half-space as a model for volcanic stressing. *Journal of Geophysical Research*, *93*(B5), 4249–4257. https://doi.org/10.1029/JB093iB05p04249